

Geochemistry, Geophysics, Geosystems

RESEARCH ARTICLE

10.1029/2019GC008270

Key Points:

- Strain partitioning between recrystallized grains and stiff quartz porphyroclasts
- Fracturing and fluid ingress assist propagation of shear bands
- Authigenesis of new quartz and phyllosilicate grains from circulating fluids promotes strain localization on shear bands

Correspondence to:

S. Papeschi,
s.papeschi@gmail.com

Citation:

Papeschi, S., & Musumeci, G. (2019). Fluid-assisted strain localization in quartz at the brittle/ductile transition. *Geochemistry, Geophysics, Geosystems*, 20, 3044–3064. <https://doi.org/10.1029/2019GC008270>



Received 12 FEB 2019

Accepted 22 MAY 2019

Accepted article online 29 MAY 2019

Published online 25 JUN 2019

Fluid-Assisted Strain Localization in Quartz at the Brittle/Ductile Transition

Samuele Papeschi^{1,2}  and Giovanni Musumeci^{2,3} 

¹Dipartimento di Scienze della Terra, Firenze University, Firenze, Italy, ²Dipartimento di Scienze della Terra, Pisa University, Pisa, Italy, ³Istituto Nazionale di Geofisica e Vulcanologia, Pisa, Italy

Abstract A mylonitic quartzite with conjugate and synthetic shear bands was investigated by Electron Backscatter Diffraction and optical microscopy to obtain insights on recrystallization mechanisms and strain localization in quartz at plastic to semibrittle conditions close to the brittle-ductile transition. The mylonitic quartzite deformed during late Miocene thrusting coeval with contact metamorphism in the high-strain domains of the Calamita Schists (Elba Island, Italy). Mylonitic deformation occurred from amphibolite to lower greenschist facies conditions during cooling of the aureole. Dynamic recrystallization, dominated by the activity of dislocation creep by prism $\langle a \rangle$ slip, produced recrystallized quartz layers mantling relic large quartz porphyroclasts. Under decreasing temperature and fluid-rich conditions, quartz porphyroclasts acted as relatively rigid bodies and fractured along synthetic and conjugate C' shear bands. Shear bands developed along kinematically favored orientations, just locally assisted by weak crystallographic planes in quartz. Fracturing along shear bands was assisted by cataclasis and fluid infiltration enhancing fracture propagation and healing by recrystallization and authigenesis of new quartz and phyllosilicate grains. The process enhanced the propagation of and strain localization in shear bands, with the development of bands of *weak* phyllosilicates. Furthermore, we observed the development of a c axis preferred orientation (CPO) related to dissolution and precipitation of new grains with their c axis oriented parallel to shear bands. This study highlights the importance of the interplay between brittle and crystal-plastic processes and fluid ingress in the semibrittle regime to understand deformation partitioning and strain localization.

Plain Language Summary Quartz is one of the main constitutive minerals of the Earth's rocks and largely controls how rocks deform. We used the optical microscope to investigate quartz and a special technique called Electron Backscatter Diffraction, which is based on the interaction between a beam of electrons and a crystalline material, to generate maps of how quartz crystals are oriented in space, in order to investigate quartz deformation. We studied rocks that were heated up to 650 °C 6 million years ago by a chamber of molten magma and at the same time were squeezed by tectonic forces in the Calamita peninsula (Elba Island, Italy). During cooling from such high temperatures, deformation in quartz was first accommodated by plastic mechanisms, like metal warped by a blacksmith, producing large quartz crystals wrapped by newly formed smaller quartz crystals. Subsequently, at lower temperatures (~300–400 °C), deformation in cool large quartz crystals started to produce cracks and fractures. As fractures opened, high-temperature water-rich fluids flooded the fractures, encrusting them with tiny quartz and platy mica crystals. This process progressively leads to the development of bands of *weak* platy micas in *hard* quartz crystals.

1. Introduction

Deformation in shear zones is accommodated by brittle, frictional mechanisms in the upper crust and by plastic mechanisms at higher temperature in the lower crust. The transition between purely brittle to purely crystal-plastic deformation in natural shear zones occurs over a wide range of temperature conditions at which deformation is controlled by a combination of brittle and plastic mechanisms (semibrittle deformation; Evans & Kohlstedt, 1995; Kohlstedt et al., 1995). A classic example is represented by sheared quartz-feldspar aggregates at midcrustal conditions, where quartz typically recrystallizes and feldspar forms fractured porphyroclasts (Tullis et al., 1990, 2000; Vernon & Flood, 1988). Quartz at midcrustal conditions (300–450 °C) is typically thought to deform by dislocation creep (Behr & Platt, 2011, 2014; Gleason & Tullis, 1995; Hirth & Tullis, 1994; Stipp et al., 2002). However, many studies, focused on quartz

monomineralic aggregates, highlighted the complex role played by grain-scale strain partitioning in assisting semibrittle deformation in quartz (van Daalen et al., 1999; Muto et al., 2011; Vernooij, Kunze, et al., 2006; Vernooij, den Brok, et al., 2006). Intragrain deformation bands in quartz, typically constituted by trails of small grains hosted by larger grains, have been classically described as the result of the interplay between brittle and crystal-plastic processes. Their development has been alternatively explained as the result of failure along the rhomb planes of quartz (van Daalen et al., 1999; Vernooij, Kunze, et al., 2006; Vernooij, den Brok, et al., 2006), conjugate kinking caused by basal $\langle a \rangle$ slip (Nishikawa & Takeshita, 1999), nucleation, and growth from highly damaged zones during a sequence of low-temperature plasticity and subsequent recrystallization (Trepmann et al., 2007; Trepmann & Stöckhert, 2003) or localized coaxial deformation in *stiff* domains (Menegon et al., 2008). Several contrasting mechanisms have been proposed to explain the growth of new grains in such bands: (1) subgrain rotation followed by rigid-body rotation of grains (Bestmann & Prior, 2003; Ceccato et al., 2017; Trepmann et al., 2017); (2) cataclasis and healing by recrystallization (den Brok, 1992; van Daalen et al., 1999; Vernooij, Kunze, et al., 2006; Vernooij, den Brok, et al., 2006); (3) dissolution-precipitation creep, with solution of material, which reprecipitates as new grains (Hippertt & Egydio-Silva, 1996; Kjöll et al., 2015; Takeshita & El-Fakharani, 2013; Takeshita & Hara, 1998); and (4) recrystallization along mechanically formed Dauphiné twins (Menegon et al., 2011; Stipp & Kunze, 2008). These structures have also been shown to form during the earthquake cycle immediately below the brittle-ductile transition (Trepmann & Stöckhert, 2003; Trepmann et al., 2007, 2017).

In this study, we present an Electron Backscatter Diffraction (EBSD)-based investigation of the development and evolution of intragrain shear bands in quartz in the semibrittle regime, investigated in a natural study case represented by a cooling contact aureole (Papeschi et al., 2017, 2018). The research presented here highlights how grain-scale contrasts drive strain partitioning from the early stages of dynamic recrystallization to the brittle regime and how the interplay between brittle and crystal-plastic processes with intergranular fluids may assist softening and strain localization in shear bands that may efficiently act as precursory structures for discrete faults.

2. Geological Outline

Elba Island, located in the northern Tyrrhenian Sea, exposes a complete cross section through the hinterland sector of the northern Apennines belt. The nappe pile is characterized by east verging structures stacked over west dipping top-to-the-E thrust sheets during the early Miocene (Keller & Coward, 1996; Massa et al., 2017). The nappe stack comprises an Upper Complex, characterized by ophiolite-bearing oceanic and continental units with anchizone to lower greenschist facies metamorphism, and a Lower Complex, consisting of the upper greenschist to amphibolite facies Ortano and Calamita Units (Figure 1a). Blueschist facies metamorphism related to early Miocene underthrusting and nappe stacking is locally preserved in the Ortano Unit (Bianco et al., 2015). However, the dominant metamorphic imprint is the late Miocene LP/HT metamorphism related to the emplacement of granitic bodies, coeval with the late phase of east verging thrusting (Duranti et al., 1992; Musumeci et al., 2015; Musumeci & Vaselli, 2012; Viola et al., 2018).

The Calamita Schists, part of the Calamita Unit (Figure 1a), are an amphibolite facies metapsammitic complex that crop out in SE Elba Island (Barberi et al., 1967). These rocks experienced Miocene deformation and LP/HT metamorphism triggered by the intrusion of the buried Porto Azzurro pluton (Papeschi et al., 2017) with peak temperatures around 625 °C (Caggianelli et al., 2018) or exceeding 650 °C (Musumeci & Vaselli, 2012) at pressure lower than 0.2 GPa (Duranti et al., 1992). Deformation, related to the activity of thrust sheets coeval with pluton emplacement, affected the Calamita Schists at upper crustal conditions during postmagmatic cooling. Geochronological data constraint ductile shearing between 6.8 and 6.3 Ma (Musumeci et al., 2015) and the subsequent brittle deformation between 6.1 and 4.9 Ma (Viola et al., 2018), indicating that the equilibration to upper crustal temperature occurred in less than 1 Ma. Deformation was heterogeneously distributed in top to the east ductile shear zones that recorded the transition from an upper amphibolite facies foliation to a greenschist facies mylonitic foliation, overprinted at the brittle/ductile transition by brittle fault zones and shear fractures. These latter crosscut the mylonitic foliation exploiting precursory ductile shear bands (Papeschi et al., 2017, 2018).

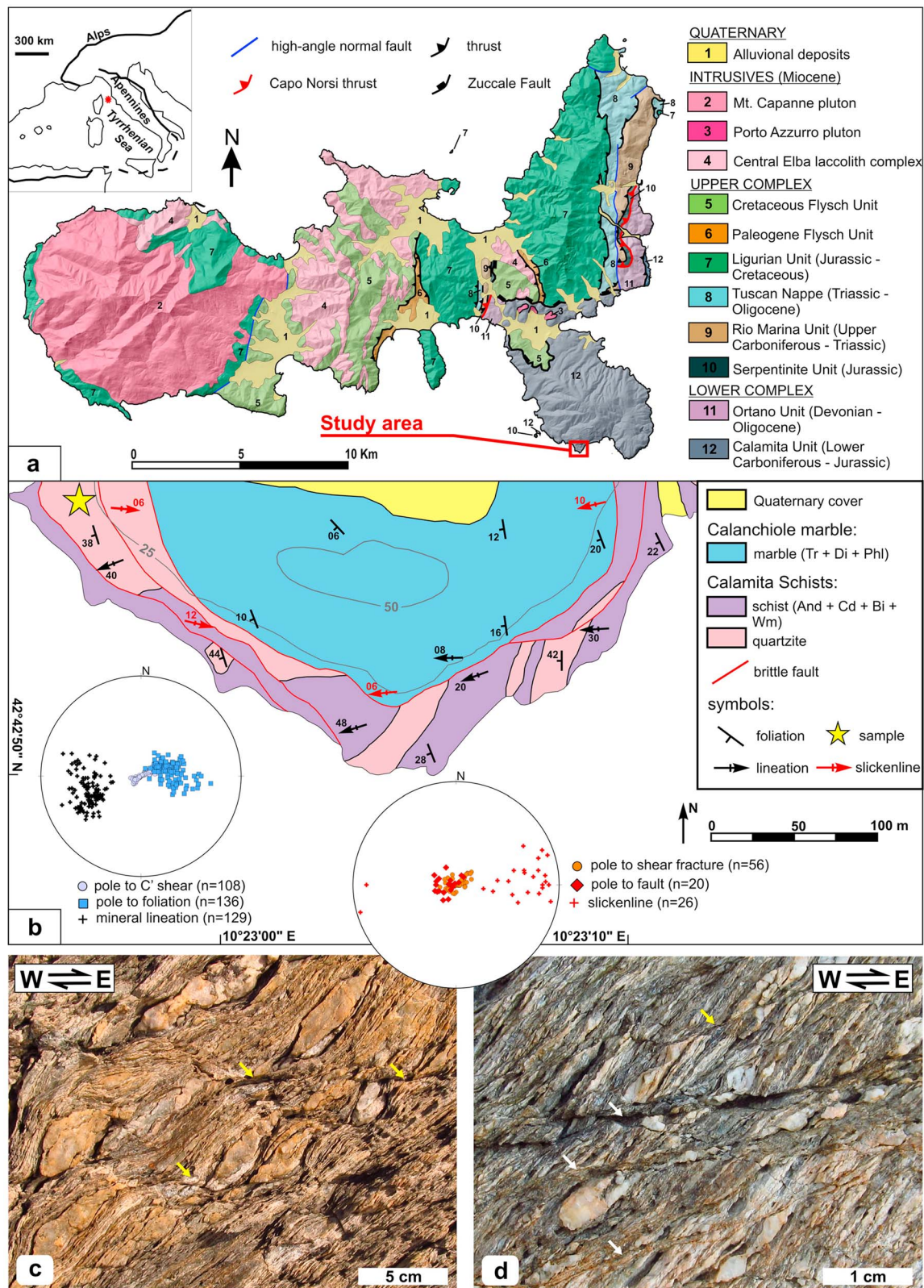


Figure 1. (a) Simplified geological map of the Elba Island (modified after Massa et al., 2017) showing the location of the study area. (b) Sketch structural-geological map of the study area (Praticciolo Cape). Insert stereographic projections are in equal angle, lower hemisphere. The yellow star marks the location of sample IESP3SP78. Mesoscale structures of the Calamita Schists at the Praticciolo: (c) well foliated top-to-the-E mylonitic micaschists with S-C' fabric and (d) top-to-the-E shear fractures cross cutting the mylonitic fabric and developed subparallel to C' shear bands. Yellow arrows: C' shear bands; white arrows: shear fractures.

The Praticciolo Cape (Figure 1b; see details in Papeschi et al., 2018) offers a natural cross section through mylonitic quartzites and micaschists belonging to the Calamita Schists, tectonically overlain by metacarbonate rocks over the flat segment of a large-scale east verging thrust (Figure 1b). Here, the Calamita Schists are characterized by a well-developed west dipping foliation (mean dip direction/dip: N261°/33°), a stretching lineation defined by quartz and phyllosilicate aggregates (trend/plunge: N255°/32°), and synthetic and conjugate sets of C' shear bands (synthetic set: N250°/03°; antithetic set: N227°/72°; Figure 1c). Shear fractures and brittle fault zones (N156°/01°), parallel to C' shear bands (Figure 1d), crosscut the foliation and represent the last deformation structures developed. For the present study, a mylonitic quartzite sample (sample IESP3SP78 highlighted in Figure 1b) has been selected for fabric analysis.

3. Analytical Method

Standard oriented thin sections (i.e., cut orthogonal to the foliation and parallel to the stretching lineation) were investigated using the optical microscope and the Scanning Electron Microscope (SEM) and for EBSD analysis of the quartz microfabric (see Prior et al., 1999).

Thin sections were polished using an alkaloid colloidal suspension (SYTON) with a Buehler Vibromet 2 for at least 3 hr and then carbon coated to about 3.5-nm thickness. EBSD maps were acquired at the Electron Microscope Centre of Plymouth University with a (1) JEOL 6610 LV SEM equipped with a NordLys Nano EBSD detector and a (2) JEOL 7001 FEG SEM equipped with a NordLys Max EBSD detector, using a 20–25-mm working distance, 70° of sample tilt with respect to the horizontal and accelerating voltage set at 20 keV. The sample symmetry used was monoclinic, and quartz was the only phase indexed, using trigonal crystal system (Laue group 3/m). EBSD patterns were automatically detected and indexed with the software AZTec (Oxford Instruments). The step size used and the size of the EBSD map frame are provided for each map in the corresponding figure. Noise reduction, following Bestmann and Prior (2003), was performed using the HKL CHANNEL 5 software (Oxford Instruments). The critical misorientation for the definition of high-angle boundaries (shown in black in orientation maps) was set at 10°, allowing grain boundary completion down to 0°, and at 2–10° for low-angle boundaries (in white). Dauphiné twin boundaries (in red; Frondel, 1962) were recognized as grain boundaries with $60^\circ \pm 2^\circ$ of misorientation and $\langle c \rangle$ as misorientation axis and disregarded from the grain detection procedure. Grain size was obtained using the grain detection routine of Channel 5 (Tango software) that recalculates grain diameters (μm) from equivalent area circles (μm^2 ; as in Berger & Herwegh, 2004). As a rule, grains measuring less than 3 times the step size (i.e., containing less than 4–9 pixels) were nullified.

Pole figures and misorientation axis orientations in sample coordinates (MOSC) are equal area, lower hemisphere projections oriented with respect to the finite strain ellipsoid reference frame (X = lineation; Z = pole to the foliation). Inverse pole figures and misorientation axis orientations in crystal coordinates (MOCC) are equal area, upper hemisphere projections. Contoured pole figures (one point per grain) were performed using 10° half width and 10° cluster size with density shown as multiples of a uniform distribution. The misorientation axis distribution in crystal coordinates (or MOCC) is a powerful tool to guess the active slip system(s) in a crystal lattice. Following Lloyd and Freeman (1994) and Neumann (2000), if we assume the ideal activity of edge dislocations associated with a slip system, the misorientation axis (i.e., axis of rotation with the smallest rotation angle among equivalent rotation relating two given orientations of an object; Morawiec, 2004) is (1) contained in the slip plane and (2) oriented perpendicular to the Burgers vector. A scheme showing the misorientation axes and related slip systems for quartz (after Neumann, 2000) is reported in Figure 2.

4. Microstructural and EBSD Analysis

4.1. Sample Description

The investigated mylonitic quartzite sample (IESP3SP78; Figure 1b) shows a well-developed foliation (oriented N220°/24°) defined by the subparallel disposition of quartz and phyllosilicate layers (Figure 3a). The kinematics is top-to-the-E, defined by asymmetric objects at the mesoscale and microscale and by S - C' structures. The foliation is cut and offset by two sets of C' shear bands: a dominant top-to-the-E set ($C'1$),

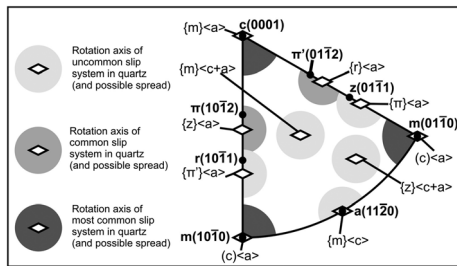


Figure 2. Sketch illustrating the relationships between position of misorientation axis clustering in crystal coordinates and rotation axis of uncommon (light grey), common (grey), and most common (dark grey) slip systems in quartz. Modified after Neumann (2000).

subhorizontal and synthetic with respect to the sample kinematics, and a less developed top-to-the-W antithetic set, which is steeply dipping at the mesoscale ($N227^\circ/72^\circ$).

At the microscale, phyllosilicate layers are very fine grained ($\ll 5 \mu\text{m}$) and almost exclusively constituted by sericite and chlorite mixed with tiny ($< 5\text{-}\mu\text{m}$) quartz grains and accessory ilmenite and magnetite that surround fractured and sericitized andalusite and cordierite porphyroclasts ($50\text{--}200 \mu\text{m}$). Large chlorite stacks (up to $200 \mu\text{m}$), biotite relics, and white mica grains (grain size: $10\text{--}100 \mu\text{m}$) are locally preserved in coarse-grained quartz lenses.

Quartz shows a strongly heterogeneous microstructure, consisting of a variable percentage of relic quartz porphyroclasts, either organized in lenses (e.g., Figure 3b) or present as isolated grains lacking a clear preferred orientation (e.g., Figure 3c), surrounded by aggregates (e.g., Figure 3c) and well-defined subparallel layers of recrystallized quartz grains (e.g., Figure 3a). Because of the marked microstructural differences observed within the quartz layers, we have studied in detail several domains, each characterized by

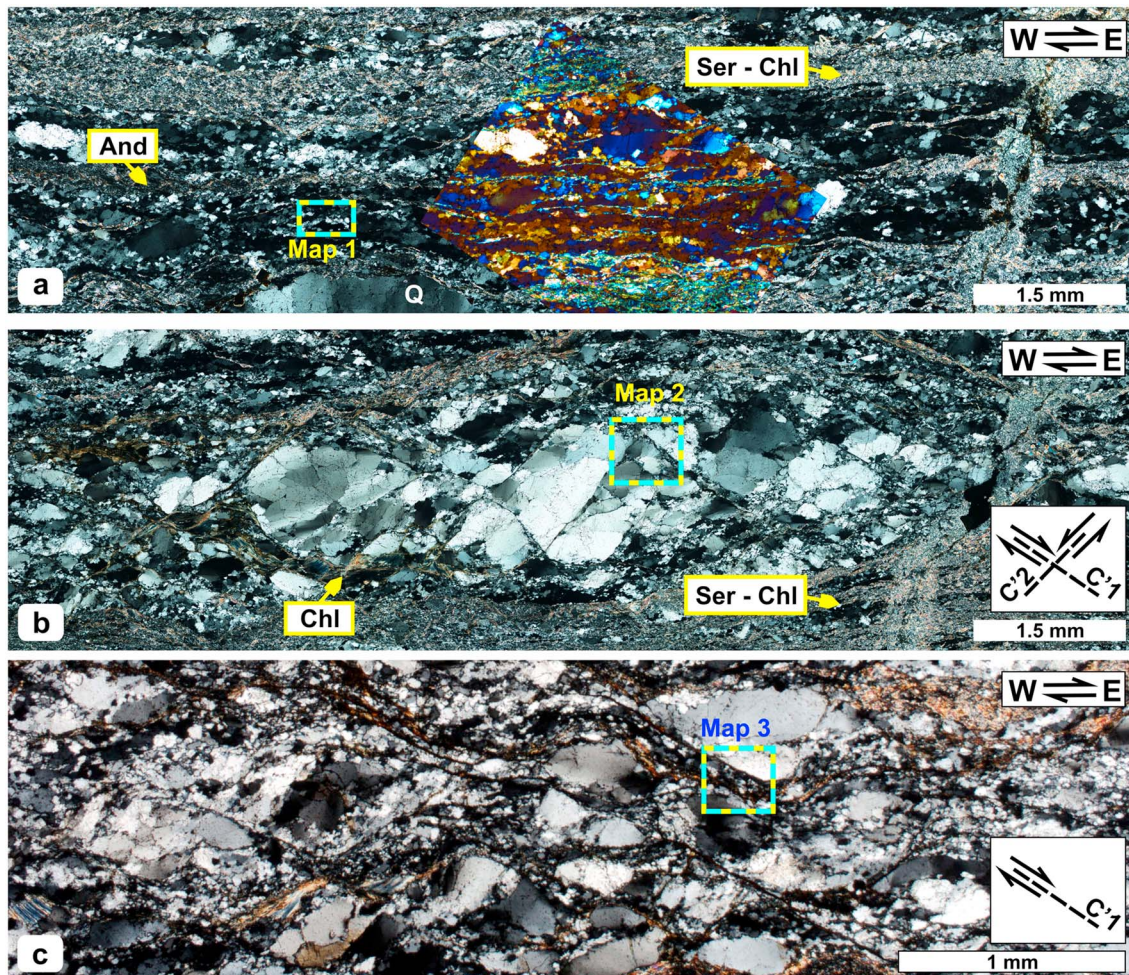


Figure 3. Microstructures of the investigated sample collected at crossed polarizers. The yellow-cyan boxes highlight the location of EBSD maps. And: andalusite; Chl: chlorite; Q: quartz; Ser: sericite. (a) Domain 1: recrystallized subparallel quartz layers interlayered with mica domains and containing large quartz porphyroclasts. The gypsum plate insert highlights the c axis orientation. (b) Domain 2: relic lens of quartz porphyroclasts surrounded by smaller recrystallized grains and crosscut by conjugate shear bands ($C'1$ and $C'2$). (c) Domain 3: large quartz porphyroclasts surrounded by recrystallized grains, eastwardly dragged along numerous synthetic C' shear bands.

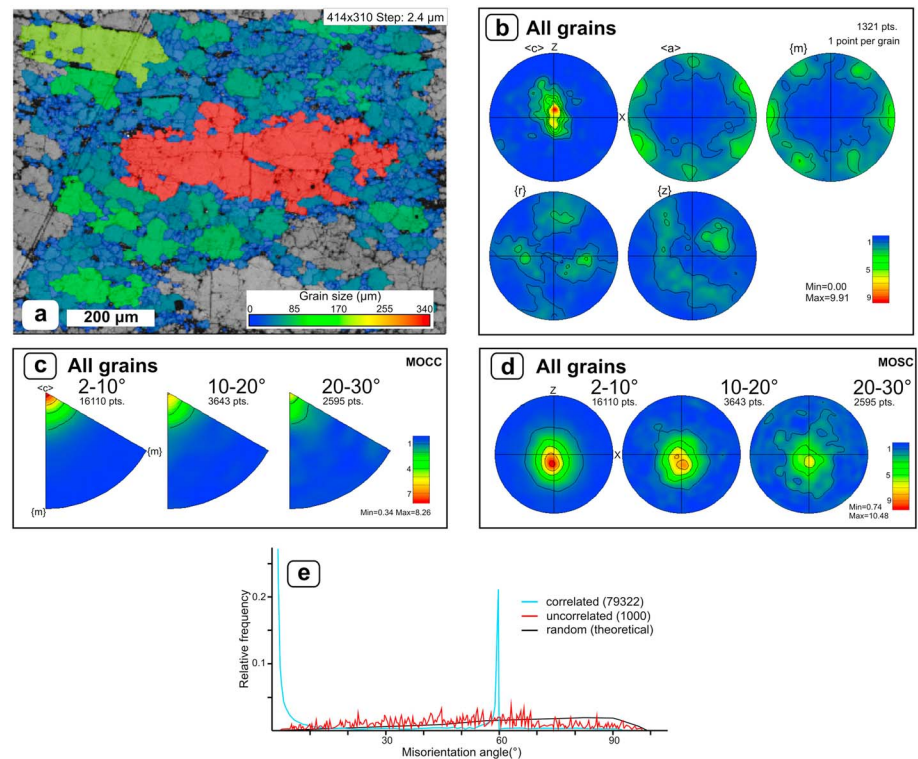


Figure 4. EBSD analysis of Domain 1. (a) Grain size map colored in respect to the legend shown in the lower right corner. (b) Contoured one-point-per-grain pole figures showing the distribution of $\langle c \rangle$ and $\langle a \rangle$ axes and poles to $\{m\}$, $\{r\}$, and $\{z\}$ planes for the complete data set. (c, d) Contoured misorientation axis distribution (c) in crystal (MOCC) and (d) sample (MOSC) coordinates for 2–10°, 10–20°, and 20–30° of misorientation angle for the complete dataset. (e) Misorientation angle distribution (MAD) for correlated (light blue curve), uncorrelated (red curve), and theoretically random (black curve) distributions.

internally homogeneous microstructures. Three different domains have been identified, described individually and mapped by EBSD: Subparallel quartz layers (Domain 1; Figure 3a), (2) quartz porphyroclasts with conjugate shear bands (Domain 2; Figure 3b), and (3) quartz layers with synthetic shear bands (Domain 3; Figure 3c).

4.2. Subparallel Quartz Layers

Subparallel quartz layers (Domain 1), ranging in thickness between 50 and 500 μm , are continuous and stretched parallel to the mylonitic foliation (Figure 3a). Thin sericite bands ($\ll 5\text{-}\mu\text{m}$ grain size) and ellipsoidal phyllosilicate aggregates, the latter representing pseudomorphs over cordierite, occur interlayered with quartz (Figure 3a). C' shear bands are uncommon and, when present, are localized in the phyllosilicate-rich interlayers.

The quartz layer microstructure is dominated by small (10–100- μm) recrystallized grains with serrated grain boundaries enveloping sparse quartz porphyroclasts (up to 500 μm) with lobate boundaries and amoeboid shape variably stretched parallel to the foliation (Figure 3a). Undulose to patchy extinction patterns are common in quartz porphyroclasts. Small white mica inclusions display evidence for pinning of quartz grain boundaries. Large areas of recrystallized grains appear extinct at the same polarizer orientation, indicating the presence of a c axis CPO (see gypsum plate insert in Figure 3a).

The EBSD analysis, carried out in an area representative of Domain 1 (Map 1 in Figure 3a), images larger grains (100–300- μm grain size), interpreted as relic grains and showing amoeboid shape and relatively high aspect ratio (2–4), defining a shape-preferred orientation parallel to the foliation (Figure 4a). Such grains are surrounded by smaller new grains (10–50 μm) with equidimensional shape and serrated grain boundaries (Figure 4a). Discontinuous low-angle boundaries with lobate shape are contained in old grains and, to a lesser extent, in some of the new grains. Irregular Dauphiné twin boundaries are present in all grains.

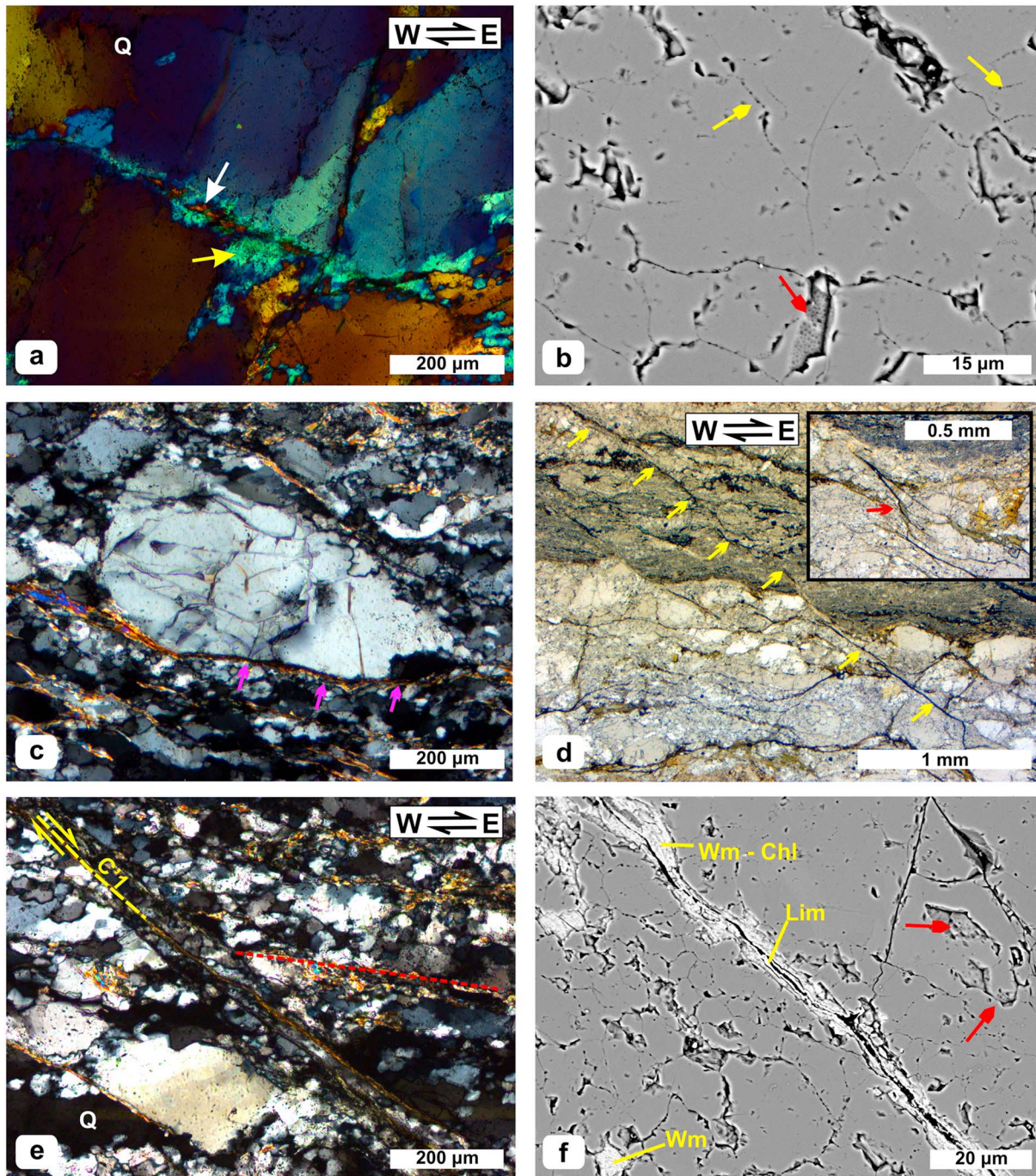


Figure 5. Microstructures of shear bands. Chl: chlorite; Lim: limonite; Q: quartz; Wm: white mica (a) conjugate shear bands hosted in large quartz porphyroclasts with small grains with similar *c* axis orientation (white arrow) and slightly misoriented damaged areas of the host grains (crossed polarizers, gypsum plate). (b) SEM BSE-image of grains localized on conjugate shear bands showing trails of fluid inclusions (yellow arrows) and pitted grain boundaries (red arrow). (c) Quartz porphyroclast in Domain 3 mantled by recrystallized grains and phyllosilicate-rich strain caps (purple arrows) showing evident internal microfracturing (crossed polarizers). (d) Shear band reactivated as a shear fracture (marked by yellow arrows) with 0.5-mm offset cross cutting the main foliation through several quartz and mica domain. The insert highlights a portion of the same shear fracture where different segments are bridged by en echelon fractures (parallel polarizers). (e) Architecture of a synthetic shear band (*C'*1; yellow dashed line) characterized by an inner core defined by small quartz grains and a well-defined band of chlorite + white mica (crossed polarizers). The red dashed line traces the foliation. (f) SEM BSE-image of a shear band core showing mica inclusions, a straight mica + chlorite + limonite band, and pitted grain boundaries (red arrows).

The bulk c axis distribution defines a Y -max with limited tails on the XZ plane, associated with $\langle a \rangle$ axes on the periphery, distributed along six regular maxima every 60° (Figure 4b). The correlated distribution in the misorientation angle distribution (MAD) shows two strong maxima, one at low-angle misorientations ($2\text{--}10^\circ$; Figure 4e) and the other for $55\text{--}60^\circ$ (Figure 4e). In crystal coordinates the misorientation axes for low misorientation angles (2 up to 30°) are clustered in correspondence of the c axis (Figure 4c). In sample coordinates, the maximum for low misorientation angles is localized defines a strong Y -max (Figure 4d).

4.3. Conjugate Shear Bands

This domain (Domain 2) is represented by quartz lenses (grain size: $100\text{--}1,000\ \mu\text{m}$; thickness: $100\text{--}200\ \mu\text{m}$ up to some mm) constituted by large quartz porphyroclasts, surrounded by recrystallized quartz grains belonging to Domain 1 (Figure 3b). Such lenses represent boudins of competent material (i.e., coarse-grained quartz) laterally bound by swells where the foliation is necked (Figure 3b). Porphyroclast quartz grains feature extensive patchy to undulose extinction and host conjugate and roughly orthogonal C' shear bands associated with irregular patterns of fractures (Figure 3b). Conjugate shear bands are strictly localized in coarse-grained quartz porphyroclast and do not affect the neighboring fine-grained quartz layers and phyllosilicate domains, as shown in Figure 3b. As shown in Figure 5a, conjugate shear bands are defined by very fine grained ($<10\text{--}20\text{-}\mu\text{m}$) trails of quartz. The host porphyroclast grains are fractured and feature fragments that have slightly different orientation (Figure 5a). The contact between host grains and shear bands is marked by slightly misoriented areas and by small quartz trails with different orientation with respect to the host and often displaying a c axis-preferred orientation (Figure 5a). At the SEM, the shear bands are characterized by fluid inclusion planes enclosing grains and cracks (Figure 5b). Pitted grain boundaries, indicative of fluid-present conditions during deformation (e.g., Mancktelow et al., 1998), are widespread (Figure 5b). Small chlorite and white mica inclusions are locally present.

A representative EBSD area was selected at the intersection of two conjugate C' shear bands hosted by quartz porphyroclasts (Map 2 in Figure 3b). The misorientation angle distribution shows high values of relative frequency for the correlated distribution, corresponding to $2\text{--}15^\circ$ and $55\text{--}60^\circ$ of misorientation, respectively (Figure 6h). The EBSD map images large ($>500\text{-}\mu\text{m}$) grains (i.e., host grains) that contains two nearly orthogonal shear bands (dextral and sinistral as shown in Figure 6a) defined by grains smaller than $50\ \mu\text{m}$ (i.e., shear band grains) and characterized by variable along-strike thickness from 150 to $10\ \mu\text{m}$ (Figure 6a). Minor shear bands decorated by few tiny grains and oriented parallel to the larger ones are also present, like the small dextral band marked by a yellow arrow in Figure 6a.

Host grains display wavy grain boundaries, locally associated with tiny grains and bulges ($5\text{--}20\ \mu\text{m}$), and irregular Dauphiné twin boundaries that are crosscut by conchoidal fractures (Figure 6a). In the pole figures, they display *single crystal* orientations, with c axes randomly clustered and $\langle a \rangle$ axes and rhombs drawing small ($20\text{--}40^\circ$) rotations, highlighting the internal distortion of the crystal lattice (Figure 6b). Shear band grains range in size between 3 and $30\ \mu\text{m}$, forming heterogeneous aggregates that envelope larger grains with variable shape and size up to $100\ \mu\text{m}$. In pole figures, shear band grains are broadly characterized by host control, as they mimic the host grains orientation, and display a c axis maximum in the upper right quadrangle of the pole figure (Figure 6c). As shown by misorientation profiles, large areas of shear band grains are slightly misoriented with respect to the host grains (less than $20\text{--}30^\circ$; Figures 6d and 6e) and just some grains are characterized by high misorientation with respect to the host (Figure 6e).

In crystal coordinates, host grains display a moderate clustering on the c axis associated with minor scattering toward the rhomb, corresponding to a weak maxima developed in the lower left quadrangle of the pole figure in sample coordinates (Figure 6f). Shear band grains show clustering of the misorientation axis in sample coordinates close to $\langle c \rangle$ with a wider spreading toward the rhombs and the prism (Figure 6g). In sample coordinates a weak maximum is present, close to Y in the upper right quadrangle of the pole figure (Figure 6g).

4.3.1. Relationships Between Shear Bands and Host Grains

The attitude of the shear bands in Map 2 was compared with the orientation of the major lattice planes within selected host grains adjacent to shear bands (subsets numbered from 1 to 4 in Figure 7a). The crystallographic orientation of the selected host grains was also compared with the crystallographic orientation of the grains associated with the dextral and sinistral shear bands (subsets highlighted in Figure 7d). The dextral shear band separates the adjacent grains 1, 2, and 3, whereas the sinistral is localized between grains 3

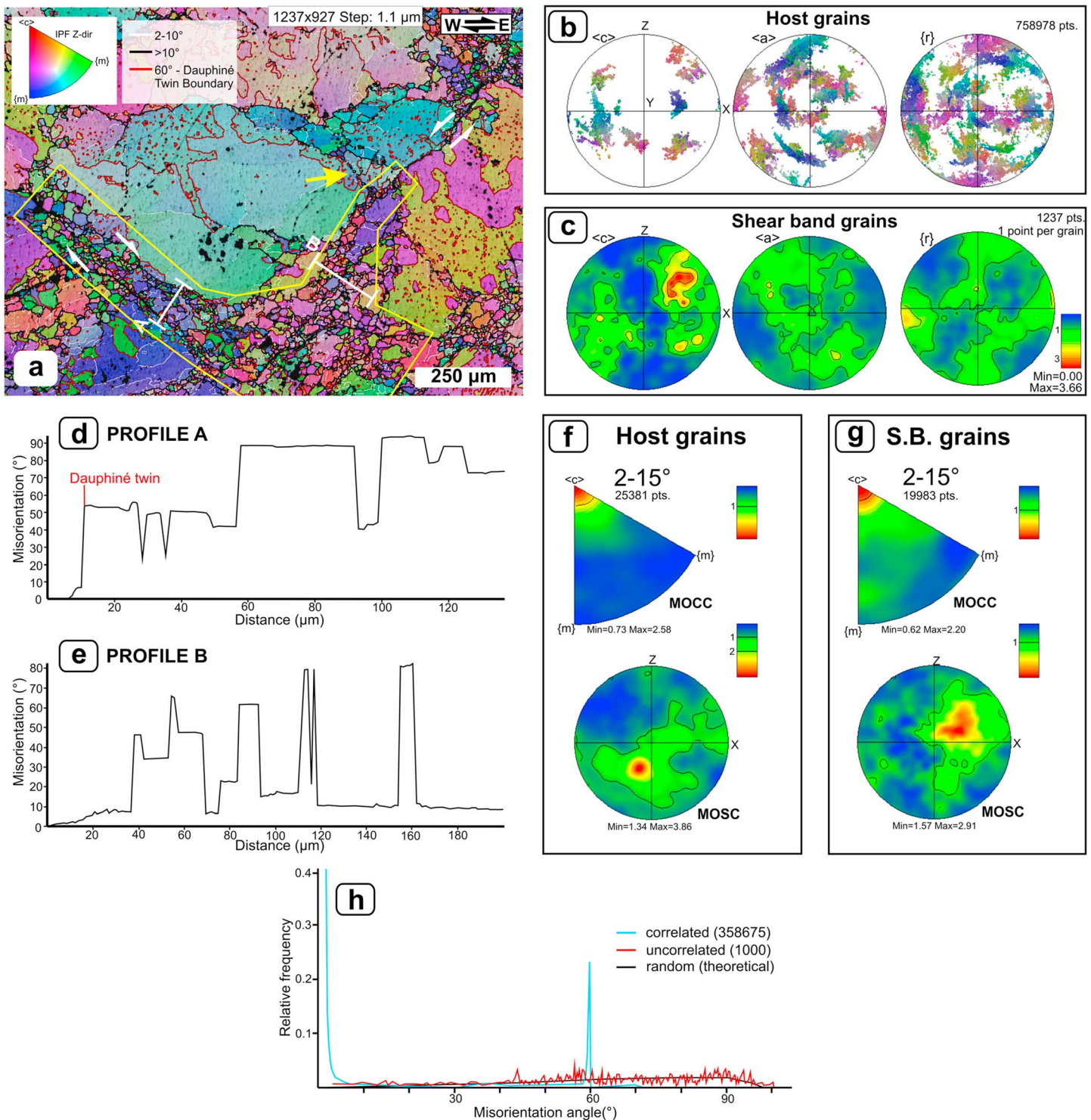


Figure 6. EBSD analysis of Domain 2. (a) Orientation map with color coding according to the inverse pole figure in the upper left corner and grain boundaries colored according to the key on top. A and B white lines correspond to misorientation profiles Figures 6d and 6e. The yellow arrow flags a small trail of recrystallized grains. White arrows mark the shear sense of conjugate shear bands. The area bound by a yellow line marks the *shear band grains* subset. (b, c) Pole figures showing the orientation of <c> and <a> axes and poles to {r} for (b) host grains and (c) shear band grains (contoured, one point per grain). (d, e) Misorientation profiles for (d) profile A and (e) profile B (location in Figure 6a). Relative misorientation with respect to the starting point plotted against distance (μm). (f, g) Contoured misorientation axis distribution in crystal (MOCC, above) and sample (MOSC, below) coordinates for 2–15° of misorientation angle for (f) host grains and (g) shear band grains subsets. (h) Misorientation angle distribution (MAD) for correlated (light blue curve), uncorrelated (red curve), and theoretically random (black curve) distributions.

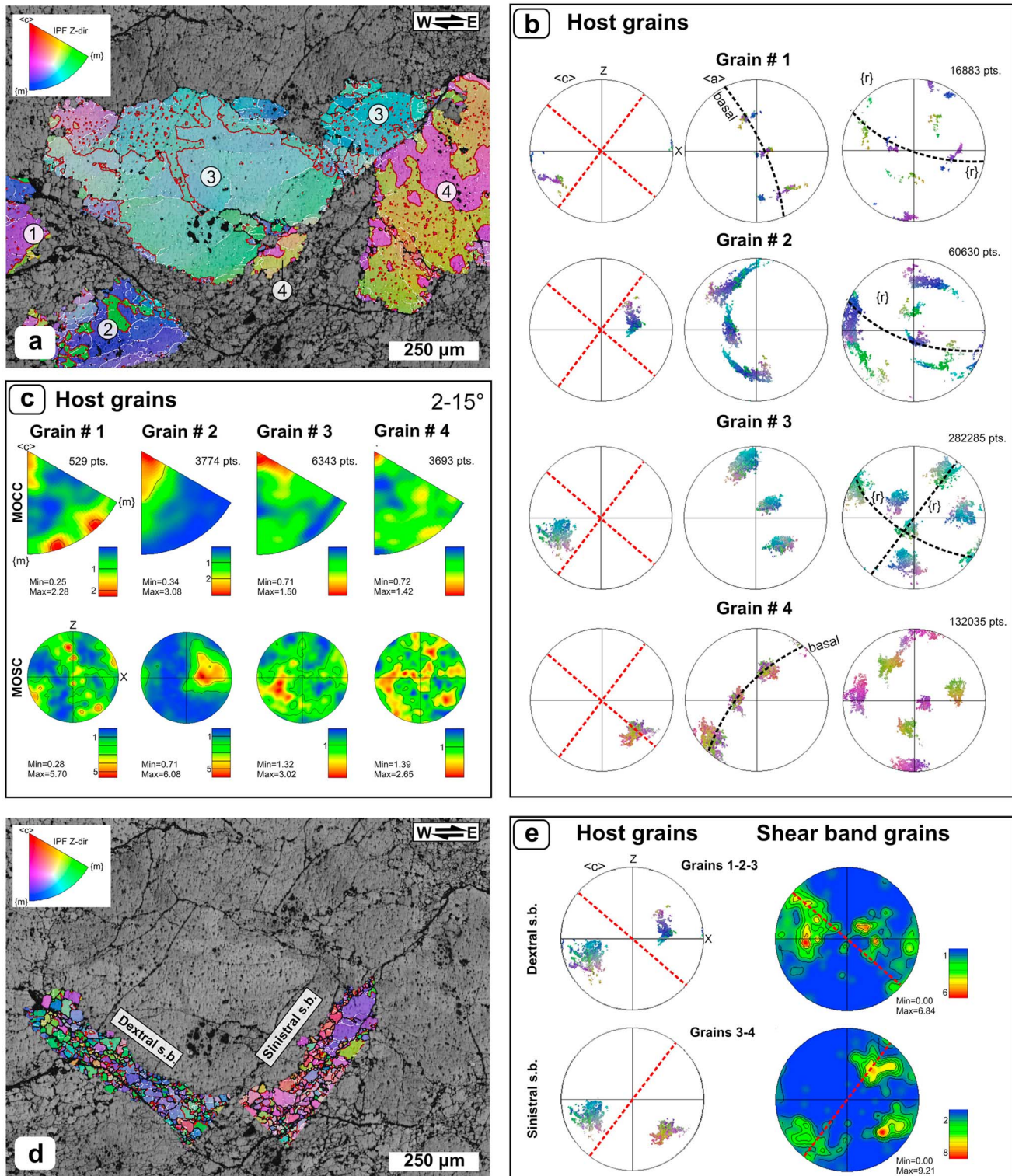


Figure 7. Relationships between host grains and shear band grains. IPF and grain boundary coloring after Figure 6a. (a) Orientation map indicating four host grains subsets, numbered from 1 to 4. (b) Pole figures showing the orientation of $\langle c \rangle$ and $\langle a \rangle$ axes and poles to $\{r\}$ for the host grains subsets. The trace of shear bands is shown with red dashed lines. Crystallographic planes that are subparallel or closely oriented to shear bands are highlighted with black dashed lines. (c) Contoured misorientation axis distribution in crystal (MOCC, above) and sample (MOSC, below) coordinates for 2–15° of misorientation angles related to the host grains subsets. (d) Orientation map highlighting the dextral and sinistral shear band subsets. (e) Comparison between $\langle c \rangle$ axis pole figures of host grains (left) and contoured one point per grain pole figures for shear band grains (right) relative to the dextral shear band (above) and the sinistral shear band (below). Red dashed lines mark the trace of C' shear bands.

and 4. Two grains with identical crystallographic orientation are present on the opposite sides of the sinistral shear band and interpreted to be originally part of the same grain (grain 4; Figure 7a).

Host grains display c axes oriented halfway between the periphery and the center of the pole figure (Figure 7b). The trace of the shear bands does not evidently match most of the crystallographic planes of the selected host grains. A slight parallelism exists only between the trace of the sinistral shear band and the positive and negative rhomb planes of grain 3 and the basal plane of grain 4 (Figure 7b). Other major crystallographic planes are oblique to shear bands. In crystal coordinates, the misorientation axis clusters in correspondence of the c axis and the acute rhombs, with minor spreading close to $\{m\}$ and $\{c\}$, as in grains 1 and 4 (Figure 7c). In sample coordinates, host grains display clustering away from Y with faint girdles (grain 1) and secondary maxima (grains 3 and 4; Figure 7c).

The comparison of the c axes of the sinistral and dextral shear band subsets (Figure 7d) with that of their respective host grains shows that the c axes of shear band grains cluster in the same orientation of those of their hosts (Figure 7e). The distribution of the c axes of shear band grains with respect to the host suggests a clockwise rotation consistent with the local, dextral (Figure 7e, above), and sinistral (Figure 7e, below) sense of shear. Considering the sinistral shear band, a third cluster is located in the upper right quadrant of the pole figure, parallel to the sinistral shear band (Figure 7e). This latter is not related to any orientation observed in the neighboring host grains and is related to grains characterized by relative misorientation up to 70–90° with respect to the hosts, that is, as the grains intercepted by misorientation profile B (Figure 6e).

4.4. Synthetic Shear Bands

Large areas of the sample are characterized by a single set of synthetic top-to-the-E C' shear bands (Domain 3), oriented ~30–35° with respect to the foliation. Differently from conjugate shear bands, synthetic shear bands do not appear restricted to coarse-grained quartz lenses but invariably affect quartz and phyllosilicate-rich layers (Figure 3c). With respect to the subparallel quartz layers (Domain 1), the quartz layers where C' shear bands are more developed appear richer in large quartz porphyroclasts (grain size: 100–500 μm) with lensoidal shape and lobate grain boundaries that are surrounded by mantles of equigranular, recrystallized grains (5–50 μm) with serrated boundaries (Figure 3c). Quartz porphyroclasts feature undulose extinction and serrated contacts with the recrystallized grains surrounding them and are often wrapped by strain caps rich in phyllosilicates or opaque mineral grains (Figure 5c). Sometimes irregular intragranular cracks are well developed in quartz porphyroclasts, dissecting angular subareas (Figure 5c). Lens-shaped quartz aggregates are commonly dragged synthetically with the shear bands, defining an $S-C'$ fabric (Figure 3c). Synthetic shear bands are often developed within or at the contact with quartz porphyroclasts with spacing lower than the millimeter and offsets that may reach several hundreds of micrometers (Figure 5d). Sometimes they are partially reactivated as small-scale shear fractures that are continuous for several millimeters through multiple mica and quartz layers characterized by millimetric offsets (Figure 5d) and bridged by en echelon subsidiary sets of fractures (Figure 5d; see insert). The shear band architecture is characterized by a 50–100- μm -thick core zone containing very fine grained quartz grains (i.e., shear band grains), locally with a shape-preferred orientation parallel to the band and a preferred orientation of the c axis, associated with bands of tiny, platy white mica and chlorite grains oriented parallel to the shear band (Figure 5e). As shown by the SEM image, the core of the shear band displays cracks and fractures associated with fluid inclusion planes and pitted quartz grain boundary surfaces (Figure 5f). Chlorite and white mica are locally associated with oxides (i.e., limonite; Figure 5f) and found as single grains included in quartz (Figure 5f). These features are indicative of fluid-rock interaction during deformation (e.g., Mancktelow et al., 1998).

The area to map by EBSD (Map 3 in Figure 3c) has been positioned within two paired, synthetic, dextral shear bands crosscutting quartz and characterized by a total offset of ~500 μm . Since quartz is the only phase indexed, phyllosilicate-rich cores appear black (Figure 8a). The large porphyroclast grains hosting the shear band (grain size >100 μm ; host grains in Figure 8; appearing gray in Figure 8d) are surrounded by small grains displaying grain size in the range 3–65 μm . The MAD shows high correlated frequencies for low angles of misorientation (<10°) and for 55–60° of misorientation (Figure 8g).

Host grains display lobate to serrated boundaries with small bulges and are characterized by wiggly Dauphiné twin boundaries and relatively straight low-angle boundaries that separate subgrains of about

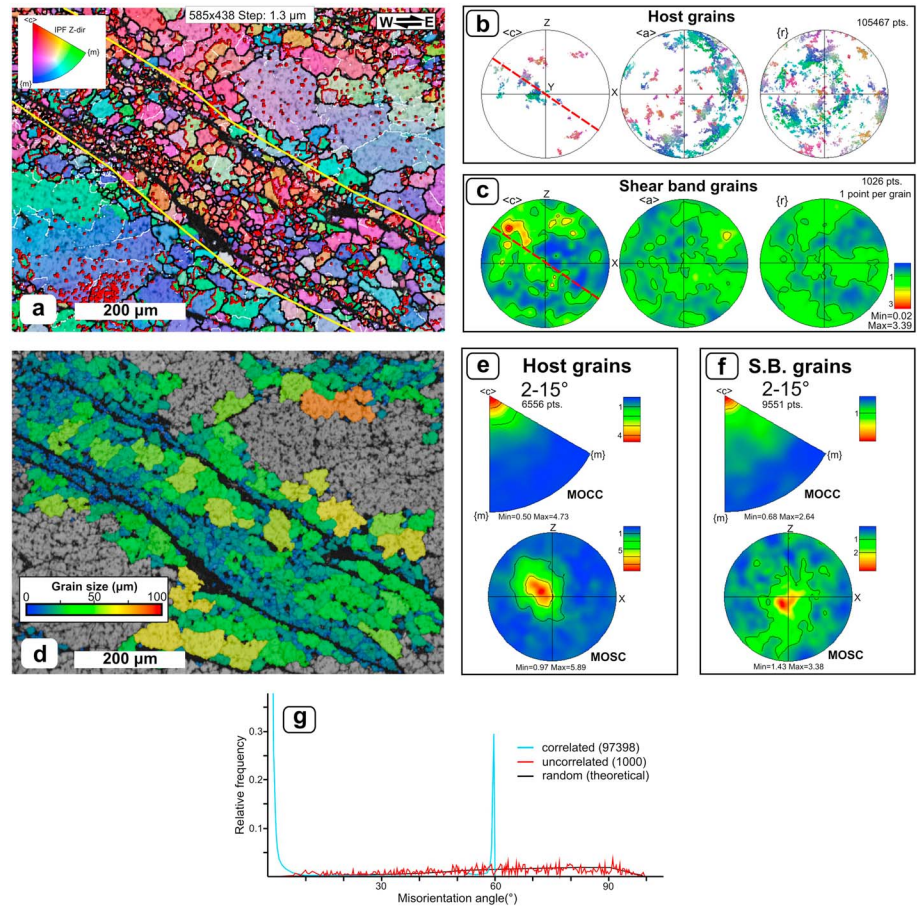


Figure 8. EBSD analysis of Domain 3. (a) Orientation map with IPF and grain boundary coloring as in Figure 4a. The yellow lines delimitate the shear band grains subset (in the center). (b, c) Pole figures showing the orientation of $\langle c \rangle$, $\langle a \rangle$ axes and poles to $\{r\}$ for (b) host grains and (c) shear band grains (contoured, one point per grain). Red dashed lines outline the trace of the shear bands. (d) Grain size distribution map showing grains with equivalent circle diameter between 0 and 100 μm , colored as in the lower left corner key. (e, f) Contoured misorientation axis distribution in crystal (MOCC, above) and sample (MOSC, below) coordinates for 2–15° of misorientation angle for (e) host grains and (f) shear band grains subsets. (g) Misorientation angle distribution (MAD) for correlated (light blue curve), uncorrelated (red curve), and theoretically random (black curve) distributions.

10–50- μm grain size (Figure 8a). The c axis of the host grains subset displays several single grain orientations scattered on the pole figure and slightly clustered close to Y (Figure 8b). Host grains are in first order mantled by new grains with equigranular shape, serrated boundaries, grain size ranging between 20 and 60 μm , and aspect ratio between 1 and 1.5–1.6 (Figure 8d).

The smaller grains of the data set (<5–20 μm ; shear band grains in Figure 8) occur localized on shear bands, largely associated with bands of phyllosilicates and characterized by an equigranular shape (Figure 8d). In the pole figure two trends are recognizable in shear band grains: (1) a contouring generally inherited from the crystal orientation of the host grains (Figure 8c; compare with Figure 8d) and (2) a strong maximum developed in the upper left quadrangle of the pole figure parallel to the shear band, in an orientation where no corresponding maximum associated with the host grains subset exists (Figure 8c).

In crystal coordinates host grains display a strong clustering for 2–15° of misorientation angles around $\langle c \rangle$, which corresponds in sample coordinates to a misorientation axis maximum clustered on Y (Figure 8e). Shear band grains are characterized in crystal coordinates by a weaker maximum with respect to the host grains clustered on $\langle c \rangle$ and a wider scattering toward the rhombs and the acute rhombs for 2–15° of misorientation angles (Figure 8f). In sample coordinates they display clustering loosely centered on Y (Figure 8f).

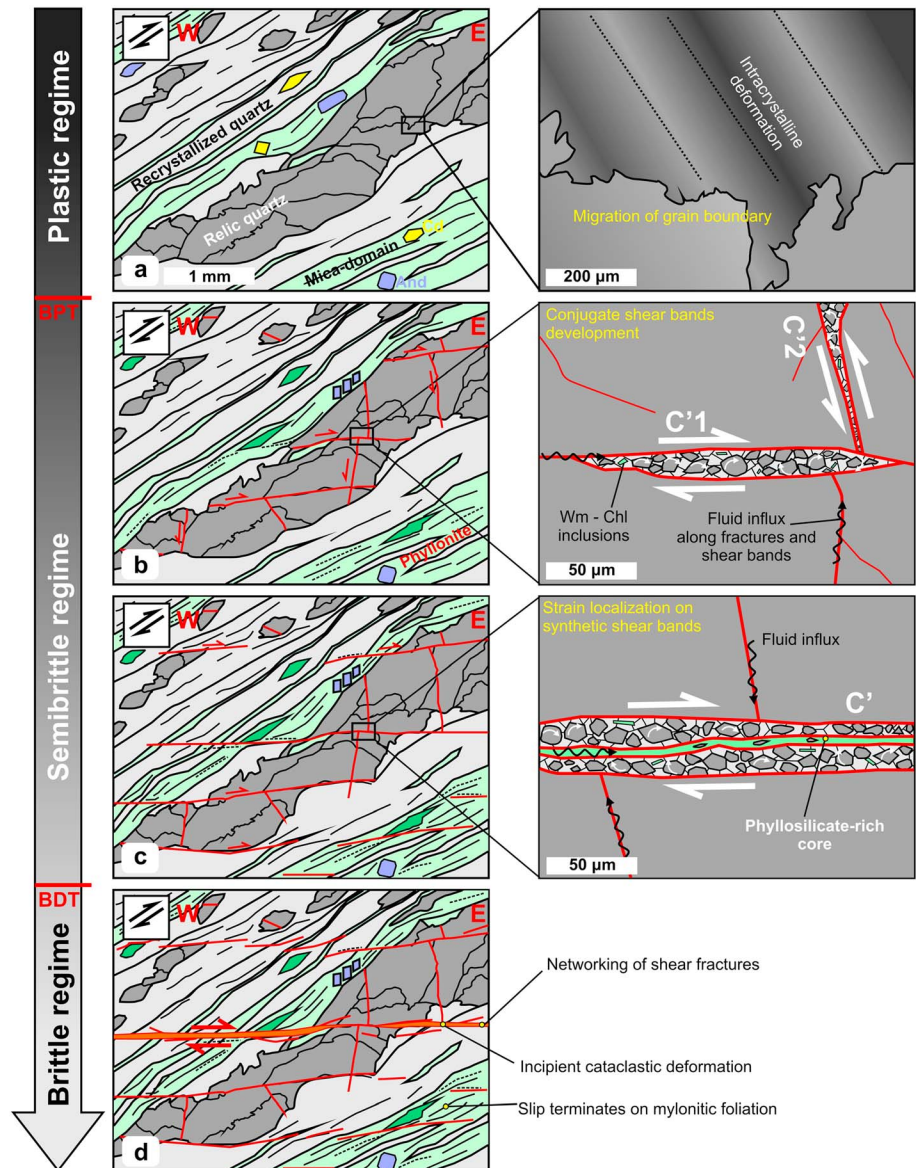


Figure 9. Sketch diagram showing the reconstructed evolution of the investigated sample in function of time and temperature decrease (dark grey to light gray arrow). BDT: brittle/ductile transition. BPT: brittle/plastic transition (definitions after Kohlstedt et al., 1995) Steps are (a) dynamic recrystallization on mylonitic ribbons leaving behind quartz porphyroclasts, (b) development of conjugate shear bands in quartz porphyroclasts, (c) strain localization on synthetic C' shear bands, and (d) reactivation of C' shear bands in the brittle regime. See text for a detailed comment.

5. Discussion

5.1. From Dynamic Recrystallization to Strain Localization in the Semibrittle Regime

The data set presented here documents the progressive development of deformation structures in a quartz-rich system at the transition from purely plastic to purely brittle deformation under fluid-rich conditions (see also Papeschi et al., 2017, 2018). The structural evolution, controlled in first order by the decreasing temperature during deformation, is conceptually summarized in Figure 9. The discussion of deformation mechanisms and processes is detailed in par. 5.2 and 5.3. At relatively high metamorphic-grade conditions (amphibolite facies; Caggianelli et al., 2018; Musumeci & Vaselli, 2012) quartz recrystallized producing stretched mylonitic ribbons (Figure 9a). Deformation concentrated in first order in recrystallized portions, leaving behind large quartz porphyroclasts, where dislocation creep was recorded as intracrystalline

deformation (Figure 9b). As temperature progressively decreased, large quartz relics underwent hardening with respect to the surrounding *soft* quartz + phyllosilicate matrix, fracturing along conjugate shear bands (Figure 9c). Opening of intragranular cracks allowed fluid infiltration and the consequent authigenesis of new quartz and phyllosilicate grains. This occurred under greenschist facies conditions, as indicated by the white mica + chlorite + opaque assemblage that is invariably found on shear bands (Figure 5), although early precursory cracking might have opened even earlier. Fluid ingress may also have aided fracture propagation by mechanisms such as stress corrosion cracking or microplasticity (Atkinson, 1984; Kerrich, 1986; Stünitz & Fitz Gerald, 1993). Transient surges in pore fluid pressure or strain rate may have also promoted fracturing and fluid ingress, followed by recrystallization and precipitation of new grains, as shown, for example, by Kjøl et al. (2015). Slip on antithetic shear bands was hindered by their steeper orientation with respect to the mylonitic foliation, promoting strain localization on the synthetic set (Figure 9d). As slip accumulated on synthetic C' shear bands, more fluids were called in, activating a positive feedback mechanism that enhanced lubrication by continuous authigenesis of soft phyllosilicates organized in subparallel bands (Figures 3c and 3d). A similar process was documented in quartz-feldspathic rocks of the South Armorican Shear Zone by Bukovská et al. (2016), who described shear band propagation by fluid infiltration promoting reaction softening at lower greenschist facies conditions.

Finally, following the embrittlement of the system below the brittle-ductile transition for quartz (i.e., 310 ± 30 °C; Stöckhert et al., 1999; 280 ± 30 °C; Stipp et al., 2002), the presence of bands of phyllosilicates in shear bands oriented obliquely to the mylonitic foliation formed a *weak* network acting as ductile precursors (Figure 1c) for faults and shear fractures (Figure 1d), as documented by Papeschi et al. (2018) and, in the studied sample, by shear fractures locally connecting and reactivating shear bands (Figure 5d). At this stage, slip on the mylonitic foliation is halted and top-to-the-E deformation starts to be accommodated by non-Andersonian faults, discordant over the foliation.

5.2. Grain-Scale Strain Partitioning in the Different Domains

Our data set documents an example of strain partitioning at the thin section scale in a quartz-dominated sample that was sheared during retrograde metamorphism from upper amphibolite to lower greenschist facies conditions. Close to peak metamorphic conditions, deformation was likely accommodated by grain boundary migration recrystallization, as indicated by relic amoeboid grains and dissection microstructures (see in detail Papeschi et al., 2017). During cooling, dynamic recrystallization by subgrain rotation and bulging led to the development of a heterogeneous microfabric generally characterized by large quartz porphyroclasts and lenses embedded in a relatively fine grained recrystallized quartz-rich matrix (Figure 3). The high frequencies shown by the correlated MAD curve for low-angle misorientations are consistent with fabric development under dominant dislocation creep (Figures 4e, 6h, and 8g). The 55–60° peak, observed in all investigated maps, is related to Dauphiné twinning. The c axis clustering with limited spreading toward the rhombs of the misorientation axis in crystal coordinates observed for both host grains and recrystallized grains in the investigated EBSD areas (Figures 4c, 6f, 6g, 8e, and 8f) is consistent with the prevailing activity of the prism $\langle a \rangle$ slip system, associated with secondary rhomb $\langle a \rangle$ slip (see Figure 2 for reference). Y -max textures, related to the activity of prism $\langle a \rangle$ slip, are consistent with upper greenschist-lower amphibolite facies deformation, assuming *normal* geologic strain rates and water content (e.g., Schmid & Casey, 1986). Though dislocation creep by prism $\langle a \rangle$ slip is witnessed in all the investigated domains, very different microstructures evolved during temperature decrease in the different domains. Two major mechanisms are believed to have controlled the development of such diverse microstructures: (1) grain-scale strain partitioning leading to a completely different microfabric evolution within the different domains and (2) fluid ingress and fluid-rock interaction, as documented by the abundant pitted grain boundaries, trails of fluid inclusions, and secondary phases trapped in quartz (Figure 5; e.g., Drury & Urai, 1990; Mancktelow et al., 1998; Mancktelow & Pennacchioni, 2004).

Domain 1, for example, is characterized by straight and parallel recrystallized quartz layers with large areas that are extinct at the same time (Figure 3a), corresponding to portions where relic and recrystallized grains contribute to define a typical Y -max texture (Schmid & Casey, 1986; Figure 4b). In this domain large relic grains were compliant during deformation developing a high aspect ratio and a preferred orientation parallel to the foliation, as it is expected for grains with c axis parallel to Y under conditions of dominant prism $\langle a \rangle$ slip (e.g., Ceccato et al., 2017; Muto et al., 2011). The favorable orientation

of the recrystallizing material assisted recrystallization at low stresses favoring the development of a strong c axis CPO (Figure 3a).

On the other hand, Domains 2 and 3 are characterized by coarse-grained relic porphyroclasts containing sets of synthetic and conjugate shear bands (Figures 3b and 3c). We suggest that such relic porphyroclasts survived during upper greenschist-amphibolite facies dynamic recrystallization, as their c axes were oriented orthogonal or oblique to Y (Figures 6b and 8b), disadvantaging dislocation creep by dominant prism $\langle a \rangle$ slip. Secondary slip systems, such as rhomb $\langle a \rangle$ (e.g., grains 2–3 in Figure 7c) or basal $\langle a \rangle$ slip (e.g., grain 1 in Figure 7c), might have been locally activated during temperature decrease, triggered by a favorable orientation of the slip system misorientation axis with respect to the vorticity axis Y (e.g., Michels et al., 2015). Nevertheless, the activation of slip systems differing from prism $\langle a \rangle$ slip was energetically unfavored at medium to high temperature and grains with c axis oriented far from Y were less stress compliant during dynamic recrystallization compared to the Y grains of Domain 1. Therefore, deformation likely concentrated in the softer, recrystallized layers that acted as the main strain-supporting framework leaving behind *hardened* coarse-grained porphyroclasts and lenses (Figures 3b and c).

During temperature decrease, large quartz porphyroclasts experienced a progressive embrittlement, concentrating strain along conjugate and synthetic shear bands.

The development of conjugate sets of shear bands in quartz has been described by several authors as a result of fracturing along planes of weakness such as the rhombs (van Daalen et al., 1999; Kjøl et al., 2015; Vernooij, Kunze, et al., 2006; Vernooij, den Brok, et al., 2006). The analysis of the shear band attitude performed by Papeschi et al. (2018) indicates a nearly constant orientation through the sample, which is not compatible with the local orientation of quartz rhomb planes. Moreover, the investigated conjugate shear bands show an orientation that is just locally parallel to the rhomb planes (Figures 7a and 7b), indicating little host control during shear band development. Conjugate shear bands in coarse-grained quartz domains may develop after deformation partitioning, as a result of coaxial deformation localizing in hard domains surrounded by a noncoaxially deforming matrix, as suggested by Menegon et al. (2008) in the Arolla Unit. Alternatively, they might be produced during general shear close to the direction of maximum shear stress or to the eigenvectors of the flow (e.g., Bobyarchick, 1986; Gillam et al., 2014; Kurz & Northrup, 2008; Simpson & de Paor, 1993), as suggested for the Calamita Schists by Papeschi et al. (2018). In this sense, the conjugate sets may preferentially nucleate in large and relatively isotropic quartz lenses, as the presence of a strong mechanical anisotropy (i.e., the mylonitic foliation) outside inhibits the development of the steeper set, as shown by Cobbold et al. (1971), Cobbold (1976), and Platt and Vissers (1980).

Propagation of shear bands outside of the coarse and stiff quartz porphyroclasts might have been promoted by temperature decrease. The presence of strong Y -max textures possibly hindered dislocation creep by basal $\langle a \rangle$ slip, which should be energetically favored at low-temperature conditions (geometric hardening; Poirier, 1980; Toy et al., 2008), forcing early strain localization in phyllosilicate-rich layers and shear bands. This might be a local effect in the Calamita Schists, as several papers documented that in retrograde shear zones, domains that deformed by basal $\langle a \rangle$ and rhomb $\langle a \rangle$ slip tend to be relatively narrow compared to the domains, which registered higher-temperature prism $\langle a \rangle$ deformation, as a result of strain localization during decreasing temperature (see, e.g., Shigematsu & Yamagishi, 2002; Shigematsu et al., 2009; Czertowicz et al., 2019). Therefore, domains that deformed by basal $\langle a \rangle$ slip might be present in the Calamita Schists and possibly have registered a different evolution at low metamorphic-grade conditions.

5.3. Role of Fluids and Dynamic Recrystallization in Shear Band Development

Formation of shear bands at greenschist to amphibolite facies conditions has classically been associated with a combination of brittle and crystal-plastic processes (Berthé et al., 1979; van Daalen et al., 1999; Gapais & White, 1982; Gapais, 1989; Passchier, 1984; Nishikawa & Takeshita, 1999; Vernooij, Kunze, et al., 2006; Vernooij, den Brok, et al., 2006). In the present study case, evidence for intragranular microcracking is invariably found as fractures and fluid inclusion planes (Figures 3b, 5b, 5c, and 5f) in quartz porphyroclasts that occur in strict association with conjugate and synthetic shear bands. Cataclasis, accompanied by rigid-body rotation of host quartz grains fragments, may explain the weak misorientation of shear band grains with respect to the host, highlighted by pole figures (Figures 6c and 8c) and by misorientation profiles (Figures 6d and 6e), and the inhomogeneous grain size of shear band grains (Figures 6a and 8d). Rigid-

body rotation is also consistent with the local clockwise and anticlockwise rotation of shear band grains with respect to the host in sinistral and dextral shear band respectively (Figure 7e). Host grains are characterized by a distorted lattice with clustering on $\langle c \rangle$ in crystal coordinates, indicative of dominant prism $\langle a \rangle$ slip, centered on Y in sample coordinates (Figures 6f and 8e). These patterns are largely inherited as intracrystalline features by shear band grains, although there is evidence of an increased activity of rhomb $\langle a \rangle$ slip (Figures 6g and 8f; see Figure 2 for reference). After microcracking and rigid-body rotation, fluid ingress might have favored dynamic recrystallization and healing of microcracks, sealing deformation in the shear band. Evidence for fluid-accompanied fracturing is supported by the presence of pitted grain boundaries and trails of fluid inclusions (Figure 5b), as well as many secondary phases trapped in quartz (Figures 5e and 5f; see, e.g., Drury & Urai, 1990; Mancktelow et al., 1998; Mancktelow & Pennacchioni, 2004). Fracturing and dynamic recrystallization might have possibly interplayed cyclically within shear bands (see, e.g., Kjöll et al., 2015), with cracking assisting fluid ingress and rapidly followed by dynamic recrystallization as described by van Daalen et al. (1999) in the Glarus Nappe and experimentally by Vernooij, Kunze, et al. (2006), Vernooij, den Brok, et al. (2006). Contrarily to van Daalen et al. (1999), however, we observed a sequence of fracturing followed by recrystallization under decreasing temperature starting from previous, higher metamorphic-grade conditions. This sequence suggests that localized fracturing was caused by strain hardening in the first place, while subsequent softening, localized on the shear bands and caused by fluid ingress, allowed recrystallization to take place.

Nevertheless, dynamic recrystallization under low-grade conditions is unable to explain the nucleation of very fine grained new grains showing c axis CPOs oriented parallel to the shear bands (Figures 6c and 8c). Such a c axis CPO would require the dominant activity of prism $\langle c \rangle$ slip, which is not supported by our data set and that is not typical under low metamorphic-grade conditions (Mainprice et al., 1986; Schmid & Casey, 1986). Furthermore, this c axis CPO is observed in grains that are strongly misoriented with respect to the host (up to 70° in misorientation profiles; Figures 6d and 6e) and does not appear to be inherited from the host grains population (Figure 7e). Strong c axis CPOs have been documented in quartz aggregates deformed at low to very low metamorphic grade, for example, in slates and schists (Stallard & Shelley, 1995; Takeshita & Hara, 1998), phyllonites (Hippertt, 1994), and veins (Cox & Etheridge, 1983). These authors explained the presence of c axis CPOs oriented parallel to the stretching lineation as a result of competitive growth during dissolution and precipitation with quartz grains growing faster along the c axis and hence showing a tendency to mark the stretching direction (Bons & den Brok, 2000; Frondel, 1962; Hippertt, 1993; Stallard & Shelley, 1995). At the same time, pressure solution preferentially removes grains with c axis parallel to the shortening direction (Becker, 1995; Hippertt, 1994). Furthermore, Stallard and Shelley (1995) and van Daalen et al. (1999) suggested that the rigid-body rotation of quartz grains, which are naturally elongated along the c axis, may help to produce a c axis CPO parallel to the foliation and/or the stretching lineation. On the other hand, c axis CPOs perpendicular to micro shear bands have been interpreted as evidence of basal $\langle a \rangle$ slip following or assisting fracturing and rigid-body rotation (e.g., van Daalen et al., 1999; Domain 2 of Kjöll et al., 2015; DAV shear zone example of Trepmann et al., 2017).

We suggest that the c axis CPO in our investigated sample was caused by the preferred growth of quartz grains with c axes parallel to shear bands, likely controlled by the opening of small dilatant sites during deformation, as shown, for example, by Hippertt (1993) and Stallard and Shelley (1995). Rigid-body rotation might have assisted the development of such a CPO (e.g., van Daalen et al., 1999). The process might have been assisted by coeval pressure solution (e.g., Figure 5c), which might have preferentially removed small quartz grains with c axis perpendicular to the shear bands (e.g., Hippertt, 1994) and readily redeposited new quartz grains sealing the shear bands. In our study case, evidence supporting extensive basal $\langle a \rangle$ slip, which might have led to c axis CPOs perpendicular to the micro shear bands, is weak (Figures 6g and 8f).

This interpretation extends previous data gathered by Takeshita and Hara (1998) and Takeshita and El-Fakharani (2013), who observed the development of weak c axis CPOs and random textures by dissolution precipitation, showing an example where precipitation of new grains from fluids may have caused the development of a c axis CPO.

The precipitation of very fine grained quartz and, in particular, weak phyllosilicates may have assisted progressive strain softening of shear bands, enhancing grain size reduction (e.g., Behrmann & Mainprice, 1987;

Fliervoet et al., 1997; White et al., 1980) and reaction softening (e.g., Bukovská et al., 2016; Stünitz & Tullis, 2001; White et al., 1980). In particular, inclusions of phyllosilicates organized in bands (Figure 5e) are widespread along synthetic C' shear bands that occur indeed not restricted to large quartz porphyroclasts (Figure 3c) and show larger eastward displacements with respect to the conjugate set. The feedback between deformation, fluid-rock interaction, and chemical processes controlled the progressive organization of phyllosilicate grains in bands on the synthetic set, promoting slip.

To summarize, the observed quartz microstructure of C' shear bands can be explained as resulting from the combination of two mechanisms: (1) microfracturing and rigid-body rotation of fragments separated from the parent grain and (2) dynamic recrystallization and healing associated with (3) authigenesis of quartz and phyllosilicate grains from circulating intergranular fluids with the development of c axis CPOs in quartz parallel to the shear bands.

5.4. Strain Localization at the Brittle/Ductile Transition

This study illustrates the complex interplay between deformation mechanisms (brittle versus crystal-plastic), recrystallization, and fluid/rock interaction that characterizes quartz-rich mylonitic rocks at low metamorphic-grade during cooling and/or exhumation. We have shown how cooling promotes general strain hardening forcing deformation partitioning between the mylonitic foliation and sets of shear bands. Such evolution is typical of low-grade quartz-feldspathic and schistose rocks and has been largely described in the recent geologic literature (Berthé et al., 1979; Bukovská et al., 2016; van Daalen et al., 1999; Gapais & White, 1982; Gapais, 1989; Gillam et al., 2014; Nishikawa & Takeshita, 1999; Vernooij, Kunze, et al., 2006; Vernooij, den Brok, et al., 2006). Other authors also documented the important role played by shear bands in crystalline basements and large shear zones that act as ductile precursors for the development of misoriented, non-Andersonian, faults (Bistacchi et al., 2012; Bolognesi & Bistacchi, 2018; Butler et al., 2008; Ikari et al., 2015; Massironi et al., 2011). However, brittle deformation is generally described as a separate event that overprints an earlier, ductile stage. We document an example of ductile-brittle shear zones, where the progressive evolution from (1) west dipping mylonites to (2) S - C mylonites with subhorizontal shear bands reactivated as faults occurred in a very short time span (<1 Ma; Musumeci et al., 2015; Papeschi et al., 2017). The described example provides clear evidence that temperature decrease forces deformation on the mylonitic foliation to concentrate into narrower and narrower domains, while slip on shear bands becomes progressively promoted in the semibrittle and brittle regime. Quartz-rich domains, which are hard during dynamic recrystallization at low metamorphic grade, may start to fracture, becoming the sites where shear bands develop. At this stage, the positive feedback mechanism between fracturing, fluid ingress, and deposition of soft phases controls the evolution of shear bands. As the system undergoes progressive embrittlement, shear bands propagate as shear fractures and finally join up to develop discrete, non-Andersonian, fault zones (e.g., Papeschi et al., 2017, 2018).

Such a progressive evolution, starting already in the ductile regime, would be facilitated under fluid-rich conditions by mechanisms such as stress-corrosion cracking (Atkinson, 1984; Kerrich, 1986; Stünitz & Fitz Gerald, 1993) and by local recrystallization (e.g., van Daalen et al., 1999). Failure along shear bands would be progressive and hence require even lower differential stress than those suggested, for example, by Bistacchi et al. (2012). We suggest that the progressive (i.e., continuous deformation) development of fault zones starting from the reactivation of ductile structures in the semibrittle regime could be a common mechanism in natural, exhuming crystalline basements, responsible for the development of non-Andersonian faults.

6. Conclusions

The microstructures presented in this paper contribute to the understanding of the switch from purely crystal-plastic to semibrittle deformation in quartz, showing how shear bands may develop and act as precursors for brittle structures. The data shown here support previous studies on the subject and add further constraints by showing the following:

- At high metamorphic-grade conditions, the dominant activity of a slip system, in this case prism $\langle a \rangle$ slip, promotes deformation in grains that are efficiently oriented for slip, leaving behind porphyroclasts that remain relatively undeformed, wrapped by the soft mylonitic matrix.

- In the semibrittle regime, deformation partitioning causes early fracturing, assisting the development of conjugate and synthetic shear bands in hard quartz porphyroclasts. The direction exploited for fracturing is not necessarily coincident with crystallographic planes of weakness but may be predetermined by the vorticity of the flow.
- Under fluid-rich conditions, fluid ingress assists propagation, healing of fractures by recrystallization, and authigenesis of new quartz and phyllosilicate grains in microfractures. The process may assist slip on shear bands, enhancing strain softening with the formation of bands of soft tiny quartz and phyllosilicates. The opening of dilatant sites during slip promoted fluid infiltration and authigenesis of quartz grains.
- Growth of quartz grains from fluids is an important mechanism for development of *c* axis CPOs parallel to shear bands under low metamorphic-grade conditions. Faster growth parallel to the *c* axis and passive rotation and dissolution of grains with unfavorable orientation together contribute to CPO development.
- Progressive strain localization on shear bands was likely favored by the geometric hardening of mylonitic ribbons and the progressive interconnection of shear band segments. In the brittle regime, slip on the mylonitic foliation is halted and deformation concentrates on the shear bands, reactivated as fault zones, discordant over the foliation.

Acknowledgments

Luca Menegon is warmly thanked for assistance and guidance with the EBSD analysis and for hosting at the Plymouth University (UK). The staff at Plymouth Electron Microscopy Centre is thanked for the technical support. Giulia degli Alessandrini, Simone Papa, and Lucy Campbell are thanked for discussion and assistance with the EBSD software. Giulio Viola and Michael Stipp are warmly thanked for their careful reviews on an earlier version of the manuscript. The constructive reviews by Toru Takeshita and an anonymous reviewer and the editorial work of Ulrich Faul are greatly acknowledged. Financial support from the University of Pisa (PRA 2016 Resp. Sergio Rocchi) and travel support from the PEGASO PhD Programme of the Tuscany Region are acknowledged. EBSD map source files are available at <https://doi.org/10.17632/8c937t6zs4.1>.

References

- Atkinson, B. K. (1984). Subcritical crack growth in geological materials. *Journal of Geophysical Research*, 89(B6), 4077–4114. <https://doi.org/10.1029/JB089iB06p04077>
- Barberi, F., Innocenti, F., & Ricci, C. A. (1967). Il complesso scistoso di Capo Calamita (Isola d'Elba). *Atti della Società Toscana di Scienze Naturali, Memorie, Serie A*, 74, 579–617.
- Becker, A. (1995). Quartz pressure solution: Influence of crystallographic orientation. *Journal of Structural Geology*, 17(10), 1395–1405. [https://doi.org/10.1016/0191-8141\(95\)00035-C](https://doi.org/10.1016/0191-8141(95)00035-C)
- Behr, W. M., & Platt, J. P. (2011). A naturally constrained stress profile through the middle crust in an extensional terrane. *Earth and Planetary Science Letters*, 303(3–4), 181–192. <https://doi.org/10.1016/j.epsl.2010.11.044>
- Behr, W. M., & Platt, J. P. (2014). Brittle faults are weak, yet the ductile middle crust is strong: Implications for lithospheric mechanics. *Geophysical Research Letters*, 41, 8067–8075. <https://doi.org/10.1002/2014GL061349>
- Behrmann, J. H., & Mainprice, D. (1987). Deformation mechanisms in a high-temperature quartz-feldspar mylonite: Evidence for superplastic flow in the lower continental crust. *Tectonophysics*, 140(2–4), 297–305. [https://doi.org/10.1016/0040-1951\(87\)90236-8](https://doi.org/10.1016/0040-1951(87)90236-8)
- Berger, A., & Herwegh, M. (2004). Grain coarsening in contact metamorphic carbonates: Effects of second-phase particles, fluid flow and thermal perturbations. *Journal of Metamorphic Geology*, 22(5), 459–474. <https://doi.org/10.1111/j.1525-1314.2004.00526.x>
- Berthé, D., Choukroune, P., & Jégouzo, P. (1979). Orthogneiss, mylonite and non coaxial deformation of granites: The example of the South Armorican Shear Zone. *Journal of Structural Geology*, 1(1), 31–42. [https://doi.org/10.1016/0191-8141\(79\)90019-1](https://doi.org/10.1016/0191-8141(79)90019-1)
- Bestmann, M., & Prior, D. J. (2003). Intragranular dynamic recrystallization in naturally deformed calcite marble: Diffusion accommodated grain boundary sliding as a result of subgrain rotation recrystallization. *Journal of Structural Geology*, 25(10), 1597–1613. [https://doi.org/10.1016/S0191-8141\(03\)00006-3](https://doi.org/10.1016/S0191-8141(03)00006-3)
- Bianco, C., Brogi, A., Caggianelli, A., Giorgetti, G., Liotta, D., & Meccheri, M. (2015). HP-LT metamorphism in Elba Island: Implications for the geodynamic evolution of the inner Northern Apennines (Italy). *Journal of Geodynamics*, 91, 13–25. <https://doi.org/10.1016/j.jog.2015.08.001>
- Bistacchi, A., Massironi, M., Menegon, L., Bolognesi, F., & Donghi, V. (2012). On the nucleation of non-Andersonian faults along phyllosilicate-rich mylonite belts. *Geological Society, London, Special Publications*, 367(1), 185–199. <https://doi.org/10.1144/SP367.13>
- Bobyarchick, A. R. (1986). The eigenvalues of steady flow in Mohr space. *Tectonophysics*, 122(1–2), 35–51. [https://doi.org/10.1016/0040-1951\(86\)90157-5](https://doi.org/10.1016/0040-1951(86)90157-5)
- Bolognesi, F., & Bistacchi, A. (2018). A km-scale “triaxial experiment” reveals the extreme mechanical weakness and anisotropy of mica-schists (Grandes Rousses Massif, France). *Journal of Structural Geology*, 107, 53–63. <https://doi.org/10.1016/j.jsg.2017.12.001>
- Bons, P. D., & den Brok, B. (2000). Crystallographic preferred orientation development by dissolution–precipitation creep. *Journal of Structural Geology*, 22(11–12), 1713–1722. [https://doi.org/10.1016/S0191-8141\(00\)00075-4](https://doi.org/10.1016/S0191-8141(00)00075-4)
- Bukovská, Z., Jeřábek, P., & Morales, L. F. (2016). Major softening at brittle-ductile transition due to interplay between chemical and deformation processes: An insight from evolution of shear bands in the South Armorican Shear Zone. *Journal of Geophysical Research: Solid Earth*, 121, 1158–1182. <https://doi.org/10.1002/2015JB012319>
- Butler, R. W. H., Bond, C. E., Shipton, Z. K., Jones, R. R., & Casey, M. (2008). Fabric anisotropy controls faulting in the continental crust. *Journal of the Geological Society*, 165(2), 449–452. <https://doi.org/10.1144/0016-76492007-129>
- Caggianelli, A., Zucchi, M., Bianco, C., Brogi, A., & Liotta, D. (2018). Estimating PT metamorphic conditions on the roof of a hidden granitic pluton: An example from the Mt. Calamita promontory (Elba Island, Italy). *Italian Journal of Geosciences*, 137(2), 238–253. <https://doi.org/10.3301/IJG.2018.11>
- Ceccato, A., Pennacchioni, G., Menegon, L., & Bestmann, M. (2017). Crystallographic control and texture inheritance during mylonitization of coarse grained quartz veins. *Lithos*, 290, 210–227.
- Cobbold, P. (1976). Mechanical effects of anisotropy during large finite deformations. *Bulletin de la Société Géologique de France*, 7(6), 1497–1510.
- Cobbold, P. R., Cosgrove, J. W., & Summers, J. M. (1971). Development of internal structures in deformed anisotropic rocks. *Tectonophysics*, 12(1), 23–53. [https://doi.org/10.1016/0040-1951\(71\)90065-5](https://doi.org/10.1016/0040-1951(71)90065-5)
- Cox, S. F., & Etheridge, M. A. (1983). Crack-seal fibre growth mechanisms and their significance in the development of oriented layer silicate microstructures. *Tectonophysics*, 92(1–3), 147–170. [https://doi.org/10.1016/0040-1951\(83\)90088-4](https://doi.org/10.1016/0040-1951(83)90088-4)

- Czertowicz, T. A., Takeshita, T., Arai, S., Yamamoto, T., Ando, J. I., Shigematsu, N., & Fujimoto, K. I. (2019). The architecture of long-lived fault zones: Insights from microstructure and quartz lattice-preferred orientations in mylonites of the Median Tectonic Line, SW Japan. *Progress in Earth and Planetary Science*, 6(1), 25. <https://doi.org/10.1186/s40645-019-0261-6>
- den Brok, S. W. J. (1992). An experimental investigation into the effect of water on the flow of quartzite. Utrecht University, Holland.
- Drury, M. R., & Urai, J. L. (1990). Deformation-related recrystallization processes. *Tectonophysics*, 172(3-4), 235–253. [https://doi.org/10.1016/0040-1951\(90\)90033-5](https://doi.org/10.1016/0040-1951(90)90033-5)
- Duranti, S., Palmeri, R., Pertusati, P. C., & Ricci, C. A. (1992). Geological evolution and metamorphic petrology of the basal sequences of eastern Elba (complex II). *Acta Vulcanologica*, 2, 213–229.
- Evans, B., & Kohlstedt, D. L. (1995). Rheology of rocks. In T. J. Ahrens (Ed.), *Rock Physics and Phase Relations: A Handbook of Physical Constants, Ref. Shelf*. (Vol. 3, pp. 148–165). Washington, DC: American Geophysical Union.
- Fliervoet, T. F., White, S. H., & Drury, M. R. (1997). Evidence for dominant grain-boundary sliding deformation in greenschist- and amphibolite-grade polymineralic ultramylonites from the Redbank Deformed Zone, Central Australia. *Journal of Structural Geology*, 19(12), 1495–1520. [https://doi.org/10.1016/S0191-8141\(97\)00076-X](https://doi.org/10.1016/S0191-8141(97)00076-X)
- Frondel, C. (1962). *The System of Mineralogy, Silica Minerals*, (7th ed., Vol. 3). New York: Wiley.
- Gapais, D. (1989). Shear structures within deformed granites: Mechanical and thermal indicators. *Geology*, 17(12), 1144–1147. [https://doi.org/10.1130/0091-7613\(1989\)017<1144:SSWDGM>2.3.CO;2](https://doi.org/10.1130/0091-7613(1989)017<1144:SSWDGM>2.3.CO;2)
- Gapais, D., & White, S. H. (1982). Ductile shear bands in a naturally deformed quartzite. *Texture, Stress, and Microstructure*, 5(1), 1–17. <https://doi.org/10.1155/TSM.5.1>
- Gillam, B. G., Little, T. A., Smith, E., & Toy, V. G. (2014). Reprint of Extensional shear band development on the outer margin of the Alpine mylonite zone, Tatare Stream, Southern Alps, New Zealand. *Journal of Structural Geology*, 64, 115–134. <https://doi.org/10.1016/j.jsg.2013.10.007>
- Gleason, G. C., & Tullis, J. (1995). A flow law for dislocation creep of quartz aggregates determined with the molten salt cell. *Tectonophysics*, 247(1-4), 1–23. [https://doi.org/10.1016/0040-1951\(95\)00011-B](https://doi.org/10.1016/0040-1951(95)00011-B)
- Hippertt, J., & Egydio-Silva, M. (1996). New polygonal grains formed by dissolution-redeposition in quartz mylonite. *Journal of Structural Geology*, 18(11), 1345–1352. [https://doi.org/10.1016/S0191-8141\(96\)00047-8](https://doi.org/10.1016/S0191-8141(96)00047-8)
- Hippertt, J. F. (1994). Microstructures and c-axis fabrics indicative of quartz dissolution in sheared quartzites and phyllonites. *Tectonophysics*, 229(3-4), 141–163. [https://doi.org/10.1016/0040-1951\(94\)90026-4](https://doi.org/10.1016/0040-1951(94)90026-4)
- Hippertt, J. F. M. (1993). 'V'-pull-apart microstructures: A new shear-sense indicator. *Journal of Structural Geology*, 15(12), 1393–1403. [https://doi.org/10.1016/0191-8141\(93\)90001-Q](https://doi.org/10.1016/0191-8141(93)90001-Q)
- Hirth, G., & Tullis, J. (1994). The brittle-plastic transition in experimentally deformed quartz aggregates. *Journal of Geophysical Research*, 99(B6), 11,731–11,747. <https://doi.org/10.1029/93JB02873>
- Ikari, M. J., Niemeijer, A. R., & Marone, C. (2015). Experimental investigation of incipient shear failure in foliated rock. *Journal of Structural Geology*, 77, 82–91. <https://doi.org/10.1016/j.jsg.2015.05.012>
- Keller, J. V. A., & Coward, M. P. (1996). The structure and evolution of the Northern Tyrrhenian Sea. *Geological Magazine*, 133(1), 1–16. <https://doi.org/10.1017/S0016756800007214>
- Kerrich, R. (1986). Fluid infiltration into fault zones: Chemical, isotopic, and mechanical effects. *Pure and Applied Geophysics*, 124(1-2), 225–268. <https://doi.org/10.1007/BF00875727>
- Kjöll, H. J., Viola, G., Menegon, L., & Sørensen, B. E. (2015). Brittle-viscous deformation of vein quartz under fluid-rich lower greenschist facies conditions. *Solid Earth*, 6(2), 681–699. <https://doi.org/10.5194/se-6-681-2015>
- Kohlstedt, D. L., Evans, B., & Mackwell, S. J. (1995). Strength of the lithosphere: Constraints imposed by laboratory experiments. *Journal of Geophysical Research*, 100(B9), 17,587–17,602. <https://doi.org/10.1029/95JB01460>
- Kurz, G. A., & Northrup, C. J. (2008). Structural analysis of mylonitic rocks in the Cougar Creek Complex, Oregon–Idaho using the porphyroblast hyperbolic distribution method, and potential use of SC'-type extensional shear bands as quantitative vorticity indicators. *Journal of Structural Geology*, 30(8), 1005–1012. <https://doi.org/10.1016/j.jsg.2008.04.003>
- Lloyd, G. E., & Freeman, B. (1994). Dynamic recrystallization of quartz under greenschist conditions. *Journal of Structural Geology*, 16(6), 867–881. [https://doi.org/10.1016/0191-8141\(94\)90151-1](https://doi.org/10.1016/0191-8141(94)90151-1)
- Mainprice, D., Bouchez, J. L., Blumenfeld, P., & Tubià, J. M. (1986). Dominant c slip in naturally deformed quartz: Implications for dramatic plastic softening at high temperature. *Geology*, 14(10), 819–822. [https://doi.org/10.1130/0091-7613\(1986\)14<819:DCSIIND>2.0.CO;2](https://doi.org/10.1130/0091-7613(1986)14<819:DCSIIND>2.0.CO;2)
- Mancktelow, N. S., Grujic, D., & Johnson, E. L. (1998). An SEM study of porosity and grain boundary microstructure in quartz mylonites, Simplon Fault Zone, Central Alps. *Contributions to Mineralogy and Petrology*, 131(1), 71–85. <https://doi.org/10.1007/s004100050379>
- Mancktelow, N. S., & Pennacchioni, G. (2004). The influence of grain boundary fluids on the microstructure of quartz-feldspar mylonites. *Journal of Structural Geology*, 26(1), 47–69. [https://doi.org/10.1016/S0191-8141\(03\)00081-6](https://doi.org/10.1016/S0191-8141(03)00081-6)
- Massa, G., Musumeci, G., Mazzarini, F., & Pieruccioni, D. (2017). Coexistence of contractional and extensional tectonics during the northern Apennines orogeny: The late Miocene out-of-sequence thrust in the Elba Island nappe stack. *Geological Journal*, 52(3), 353–368. <https://doi.org/10.1002/gj.2761>
- Massironi, M., Bistacchi, A., & Menegon, L. (2011). Misoriented faults in exhumed metamorphic complexes: Rule or exception? *Earth and Planetary Science Letters*, 307(1-2), 233–239. <https://doi.org/10.1016/j.epsl.2011.04.041>
- Menegon, L., Pennacchioni, G., Heilbronner, R., & Pittarello, L. (2008). Evolution of quartz microstructure and c-axis crystallographic preferred orientation within ductile deformed granitoids (Arolla unit, Western Alps). *Journal of Structural Geology*, 30(11), 1332–1347. <https://doi.org/10.1016/j.jsg.2008.07.007>
- Menegon, L., Piazzolo, S., & Pennacchioni, G. (2011). The effect of Dauphiné twinning on plastic strain in quartz. *Contributions to Mineralogy and Petrology*, 161(4), 635–652. <https://doi.org/10.1007/s00410-010-0554-7>
- Michels, Z. D., Kruckenberg, S. C., Davis, J. R., & Tikoff, B. (2015). Determining vorticity axes from grain-scale dispersion of crystallographic orientations. *Geology*, 43(9), 803–806. <https://doi.org/10.1130/G36868.1>
- Morawiec, A. (2004). *Misorientation Angle and Axis Distributions*. Berlin, Heidelberg: Springer.
- Musumeci, G., Mazzarini, F., & Cruden, A. R. (2015). The Zuccale Fault, Elba Island, Italy: A new perspective from fault architecture. *Tectonics*, 34, 1195–1218. <https://doi.org/10.1002/2014TC003809>
- Musumeci, G., & Vaselli, L. (2012). Neogene deformation and granite emplacement in the metamorphic units of northern Apennines (Italy): Insights from mylonitic marbles in the Porto Azzurro pluton contact aureole (Elba Island). *Geosphere*, 8(2), 470–490. <https://doi.org/10.1130/GES00665.1>

- Muto, J., Hirth, G., Heilbronner, R., & Tullis, J. (2011). Plastic anisotropy and fabric evolution in sheared and recrystallized quartz single crystals. *Journal of Geophysical Research*, 116, B02206. <https://doi.org/10.1029/2010JB007891>
- Neumann, B. (2000). Texture development of recrystallised quartz polycrystals unravelled by orientation and misorientation characteristics. *Journal of Structural Geology*, 22(11-12), 1695–1711. [https://doi.org/10.1016/S0191-8141\(00\)00060-2](https://doi.org/10.1016/S0191-8141(00)00060-2)
- Nishikawa, O., & Takeshita, T. (1999). Dynamic analysis and two types of kink bands in quartz veins deformed under subgreenschist conditions. *Tectonophysics*, 301(1-2), 21–34. [https://doi.org/10.1016/S0040-1951\(98\)00219-4](https://doi.org/10.1016/S0040-1951(98)00219-4)
- Papeschi, S., Musumeci, G., & Mazzarini, F. (2017). Heterogeneous brittle-ductile deformation at shallow crustal levels under high thermal conditions: The case of a synkinematic contact aureole in the inner northern Apennines, southeastern Elba Island, Italy. *Tectonophysics*, 717, 547–564. <https://doi.org/10.1016/j.tecto.2017.08.020>
- Papeschi, S., Musumeci, G., & Mazzarini, F. (2018). Evolution of shear zones through the brittle-ductile transition: The Calamita Schists (Elba Island, Italy). *Journal of Structural Geology*, 113, 100–114. <https://doi.org/10.1016/j.jsg.2018.05.023>
- Passchier, C. W. (1984). The generation of ductile and brittle shear bands in a low-angle mylonite zone. *Journal of Structural Geology*, 6(3), 273–281. [https://doi.org/10.1016/0191-8141\(84\)90051-8](https://doi.org/10.1016/0191-8141(84)90051-8)
- Platt, J. P., & Vissers, R. L. M. (1980). Extensional structures in anisotropic rocks. *Journal of Structural Geology*, 2(4), 397–410. [https://doi.org/10.1016/0191-8141\(80\)90002-4](https://doi.org/10.1016/0191-8141(80)90002-4)
- Poirier, J. P. (1980). Shear localization and shear instability in materials in the ductile field. *Journal of Structural Geology*, 2(1-2), 135–142. [https://doi.org/10.1016/0191-8141\(80\)90043-7](https://doi.org/10.1016/0191-8141(80)90043-7)
- Prior, D. J., Boyle, A. P., Brenker, F., Cheadle, M. C., Day, A., Lopez, G., et al. (1999). The application of electron backscatter diffraction and orientation contrast imaging in the SEM to textural problems in rocks. *American Mineralogist*, 84(11-12), 1741–1759. <https://doi.org/10.2138/am-1999-11-1204>
- Schmid, S. M., & Casey, M. (1986). Complete fabric analysis of some commonly observed quartz c-axis patterns. *Mineral and Rock Deformation: Laboratory Studies*, 36, 263–286. <https://doi.org/10.1029/GM036p0263>
- Shigematsu, N., Fujimoto, K., Ohtani, T., Shibazaki, B., Tomita, T., Tanaka, H., & Miyashita, Y. (2009). Localisation of plastic flow in the mid-crust along a crustal-scale fault: Insight from the Hatagawa Fault Zone, NE Japan. *Journal of Structural Geology*, 31(6), 601–614. <https://doi.org/10.1016/j.jsg.2009.04.004>
- Shigematsu, N., & Yamagishi, H. (2002). Quartz microstructures and deformation conditions in the Hatagawa shear zone, northeastern Japan. *Island Arc*, 11(1), 45–60. <https://doi.org/10.1046/j.1440-1738.2002.00354.x>
- Simpson, C., & de Paor, D. G. (1993). Strain and kinematic analysis in general shear zones. *Journal of Structural Geology*, 15(1), 1–20. [https://doi.org/10.1016/0191-8141\(93\)90075-L](https://doi.org/10.1016/0191-8141(93)90075-L)
- Stallard, A., & Shelley, D. (1995). Quartz c-axes parallel to stretching directions in very low-grade metamorphic rocks. *Tectonophysics*, 249(1-2), 31–40. [https://doi.org/10.1016/0040-1951\(95\)00040-T](https://doi.org/10.1016/0040-1951(95)00040-T)
- Stipp, M., & Kunze, K. (2008). Dynamic recrystallization near the brittle-plastic transition in naturally and experimentally deformed quartz aggregates. *Tectonophysics*, 448(1-4), 77–97. <https://doi.org/10.1016/j.tecto.2007.11.041>
- Stipp, M., Stünitz, H., Heilbronner, R., & Schmid, S. M. (2002). The eastern Tonale fault zone: A “natural laboratory” for crystal plastic deformation of quartz over a temperature range from 250 to 700 C. *Journal of Structural Geology*, 24(12), 1861–1884. [https://doi.org/10.1016/S0191-8141\(02\)00035-4](https://doi.org/10.1016/S0191-8141(02)00035-4)
- Stöckhert, B., Brix, M. R., Kleinschrodt, R., Hurford, A. J., & Wirth, R. (1999). Thermochronometry and microstructures of quartz—A comparison with experimental flow laws and predictions on the temperature of the brittle–plastic transition. *Journal of Structural Geology*, 21(3), 351–369. [https://doi.org/10.1016/S0191-8141\(98\)00114-X](https://doi.org/10.1016/S0191-8141(98)00114-X)
- Stünitz, H., & Fitz Gerald, J. (1993). Deformation of granitoids at low metamorphic grade. II: Granular flow in albite-rich mylonites. *Tectonophysics*, 221(3-4), 299–324. [https://doi.org/10.1016/0040-1951\(93\)90164-F](https://doi.org/10.1016/0040-1951(93)90164-F)
- Stünitz, H., & Tullis, J. (2001). Weakening and strain localization produced by syn-deformational reaction of plagioclase. *International Journal of Earth Sciences*, 90(1), 136–148. <https://doi.org/10.1007/s005310000148>
- Takeshita, T., & El-Fakharani, A. H. (2013). Coupled micro-faulting and pressure solution creep overprinted on quartz schist deformed by intracrystalline plasticity during exhumation of the Sambagawa metamorphic rocks, southwest Japan. *Journal of Structural Geology*, 46, 142–157. <https://doi.org/10.1016/j.jsg.2012.09.014>
- Takeshita, T., & Hara, I. (1998). c-axis fabrics and microstructures in a recrystallized quartz vein deformed under fluid-rich greenschist conditions. *Journal of Structural Geology*, 20(4), 417–431. [https://doi.org/10.1016/S0191-8141\(97\)00108-9](https://doi.org/10.1016/S0191-8141(97)00108-9)
- Toy, V. G., Prior, D. J., & Norris, R. J. (2008). Quartz fabrics in the Alpine Fault mylonites: Influence of pre-existing preferred orientations on fabric development during progressive uplift. *Journal of Structural Geology*, 30(5), 602–621. <https://doi.org/10.1016/j.jsg.2008.01.001>
- Trepmann, C. A., Hsu, C., Hentschel, F., Döhler, K., Schneider, C., & Wichmann, V. (2017). Recrystallization of quartz after low-temperature plasticity—The record of stress relaxation below the seismogenic zone. *Journal of Structural Geology*, 95, 77–92. <https://doi.org/10.1016/j.jsg.2016.12.004>
- Trepmann, C. A., & Stöckhert, B. (2003). Quartz microstructures developed during non-steady state plastic flow at rapidly decaying stress and strain rate. *Journal of Structural Geology*, 25(12), 2035–2051. [https://doi.org/10.1016/S0191-8141\(03\)00073-7](https://doi.org/10.1016/S0191-8141(03)00073-7)
- Trepmann, C. A., Stöckhert, B., Dorner, D., Moghadam, R. H., Küster, M., & Röller, K. (2007). Simulating coseismic deformation of quartz in the middle crust and fabric evolution during postseismic stress relaxation—An experimental study. *Tectonophysics*, 442(1-4), 83–104. <https://doi.org/10.1016/j.tecto.2007.05.005>
- Tullis, J., Dell'Angelo, L., & Yund, R. A. (1990). Ductile shear zones from brittle precursors in feldspathic rocks: The role of dynamic recrystallization. In B. E. Hobbs, & H. C. Heard (Eds.), *Mineral and Rock Deformation: Laboratory Studies, Geophysical Monograph Series*, (Vol. 56, pp. 67–81). Washington, DC: American Geophysical Union.
- Tullis, J., Stünitz, H., Teyssier, C., & Heilbronner, R. (2000). Deformation microstructures in quartz-feldspathic rocks. In M. W. Jessell, & J. Urai (Eds.), *Stress, Strain and Structure: A Volume in Honor of W.D. Means, Journal of the Virtual Explorer*, 2, paper 16. <https://doi.org/10.3809/jvirtex.2000.00019>
- van Daalen, M., Heilbronner, R., & Kunze, K. (1999). Orientation analysis of localized shear deformation in quartz fibres at the brittle–ductile transition. *Tectonophysics*, 303(1-4), 83–107. [https://doi.org/10.1016/S0040-1951\(98\)00264-9](https://doi.org/10.1016/S0040-1951(98)00264-9)
- Vernon, R. H., & Flood, R. H. (1988). Contrasting deformation of S- and I-type granitoids in the Lachlan fold belt, eastern Australia. *Tectonophysics*, 147(1-2), 127–143. [https://doi.org/10.1016/0040-1951\(88\)90152-7](https://doi.org/10.1016/0040-1951(88)90152-7)
- Vernooij, M. G., den Brok, B., & Kunze, K. (2006). Development of crystallographic preferred orientations by nucleation and growth of new grains in experimentally deformed quartz single crystals. *Tectonophysics*, 427(1-4), 35–53. <https://doi.org/10.1016/j.tecto.2006.06.008>

- Vernooij, M. G., Kunze, K., & den Brok, B. (2006). "Brittle" shear zones in experimentally deformed quartz single crystals. *Journal of Structural Geology*, 28(7), 1292–1306. <https://doi.org/10.1016/j.jsg.2006.03.018>
- Viola, G., Torgersen, E., Mazzarini, F., Musumeci, G., van der Lelij, R., Schönerberger, J., & Garofalo, P. S. (2018). New constraints on the evolution of the inner Northern Apennines by K-Ar dating of Late Miocene-Early Pliocene compression on the Island of Elba, Italy. *Tectonics*, 37, 3229–3243. <https://doi.org/10.1029/2018TC005182>
- White, S. H., Burrows, S. E., Carreras, J., Shaw, N. D., & Humphreys, F. J. (1980). On mylonites in ductile shear zones. *Journal of Structural Geology*, 2(1-2), 175–187. [https://doi.org/10.1016/0191-8141\(80\)90048-6](https://doi.org/10.1016/0191-8141(80)90048-6)